

The DECADE cosmic shear project I: A new weak lensing shape catalog of 107 million galaxies

D. Anbajagane (අනුබාගනේ)^{1,2} C. Chang^{1,2} Z. Zhang^{1,3,4} C. Y. Tan^{5,2} M. Adamow^{6,7} L. F. Secco² M. R. Becker⁸ P. S. Ferguson⁹ A. Drlica-Wagner^{10,1,2} R. A. Gruendl^{6,7} K. Herron¹¹ A. Tong¹² M. A. Troxel¹³ D. Sanchez-Cid^{14,15} I. Sevilla-Noarbe¹⁶ N. Chicoine^{1,17} R. Teixeira^{1,13} A. Alarcon¹⁸ D. Suson¹⁹ A. N. Alsina²⁰ A. Amon²¹ C. R. Bom²² J. A. Carballo-Bello²³ W. Cerny²⁴ A. Choi²⁵ Y. Choi²⁶ C. Doux²⁷ K. Eckert¹² M. Gatti² D. Gruen^{28,29} D. J. James^{30,31} M. Jarvis¹² N. Kuropatkin¹⁰ C. E. Martínez-Vázquez³² P. Massana³³ S. Mau^{3,34} J. McCullough³⁵ G. E. Medina^{36,37} B. Mutlu-Pakdil¹¹ M. Navabi³⁸ N. E. D. Noël³⁸ A. B. Pace³⁹ J. Prat⁴⁰ M. Raveri⁴¹ A. H. Riley⁴² E. S. Rykoff^{4,34} J. D. Sakowska³⁸ D. J. Sand⁴³ L. Santana-Silva²² T. Shin⁴⁴ M. Soares-Santos¹⁵ G. S. Stringfellow⁴⁵ A. K. Vivas⁴⁶ and M. Yamamoto²¹

¹ Department of Astronomy and Astrophysics, University of Chicago, Chicago, IL 60637, USA

² Kavli Institute for Cosmological Physics, University of Chicago, Chicago, IL 60637, USA

³ Department of Physics, Stanford University, 382 Via Pueblo Mall, Stanford, CA 94305, USA

⁴ SLAC National Accelerator Laboratory, Menlo Park, CA 94025, USA

⁵ Department of Physics, University of Chicago, Chicago, IL 60637, USA

⁶ Center for Astrophysical Surveys, National Center for Supercomputing Applications, 1205 West Clark St., Urbana, IL 61801, USA

⁷ Department of Astronomy, University of Illinois at Urbana-Champaign, 1002 W. Green Street, Urbana, IL 61801, USA

⁸ Argonne National Laboratory, 9700 South Cass Avenue, Lemont, IL 60439, USA

⁹ DIRAC Institute, Department of Astronomy, University of Washington, 3910 15th Ave NE, Seattle, WA, 98195, USA

¹⁰ Fermi National Accelerator Laboratory, P. O. Box 500, Batavia, IL 60510, USA

¹¹ Department of Physics and Astronomy, Dartmouth College, Hanover, NH 03755, USA

¹² Department of Physics and Astronomy, University of Pennsylvania, Philadelphia, PA 19104, USA

¹³ Department of Physics, Duke University Durham, NC 27708, USA

¹⁴ Centro de Investigaciones Energéticas, Medioambientales y Tecnológicas (CIEMAT), Madrid, Spain

¹⁵ Physik-Institut, University of Zurich, Winterthurerstrasse 190, CH-8057 Zurich, Switzerland

¹⁶ Centro de Investigaciones Energéticas, Medioambientales y Tecnológicas (CIEMAT), Madrid, Spain

¹⁷ Department of Physics and Astronomy, University of Pittsburgh, 3941 O'Hara Street, Pittsburgh, PA 15260

¹⁸ Institute of Space Sciences (ICE, CSIC), Campus UAB, Carrer de Can Magrans, s/n, 08193 Barcelona, Spain

¹⁹ Department of Chemistry and Physics, Purdue University Northwest 2200, 169th Ave, Hammond, IN 46323

²⁰ Instituto de Física Gleb Wataghin, Universidade Estadual de Campinas, 13083-859, Campinas, SP, Brazil

²¹ Department of Astrophysical Sciences, Princeton University, Peyton Hall, Princeton, NJ 08544, USA

²² Centro Brasileiro de Pesquisas Físicas, Rua Dr. Xavier Sigaud 150, 22290-180 Rio de Janeiro, RJ, Brazil

²³ Instituto de Alta Investigación, Universidad de Tarapacá, Casilla 7D, Arica, Chile

²⁴ Department of Astronomy, Yale University, New Haven, CT 06520, USA

²⁵ NASA Goddard Space Flight Center, 8800 Greenbelt Rd, Greenbelt, MD 20771, USA

²⁶ NSF National Optical-Infrared Astronomy Research Laboratory

²⁷ Université Grenoble Alpes, CNRS, LPSC-IN2P3, 38000 Grenoble, France

²⁸ University Observatory, Faculty of Physics, Ludwig-Maximilians-Universität, Scheinerstr. 1, 81679 Munich, Germany

²⁹ Excellence Cluster ORIGINS, Boltzmannstr. 2, 85748 Garching, Germany

³⁰ Applied Materials Inc., 35 Dory Road, Gloucester, MA 01930

³¹ ASTRAVEO LLC, PO Box 1668, Gloucester, MA 01931

³² International Gemini Observatory/NSF NOIRLab, 670 N. A'ohoku Place, Hilo, Hawai'i, 96720, USA

³³ NSF's NOIRLab, Casilla 603, La Serena, Chile

³⁴ Kavli Institute for Particle Astrophysics & Cosmology, P.O. Box 2450, Stanford University, Stanford, CA 94305, USA

³⁵ Department of Astrophysical Sciences, Peyton Hall, Princeton University, Princeton, NJ USA 08544

³⁶ Dunlap Institute for Astronomy & Astrophysics, University of Toronto, 50 St George Street, Toronto, ON M5S 3H4, Canada

³⁷ David A. Dunlap Department of Astronomy & Astrophysics, University of Toronto, 50 St George Street, Toronto ON M5S 3H4, Canada

³⁸ Department of Physics, University of Surrey, Guildford GU2 7XH, UK

³⁹ Department of Astronomy, University of Virginia, 530 McCormick Road, Charlottesville, VA 22904, USA

⁴⁰ Nordita, KTH Royal Institute of Technology and Stockholm University, SE-106 91 Stockholm.

⁴¹ Department of Physics and INFN, University of Genova, Genova, Italy

⁴² Institute for Computational Cosmology, Department of Physics, Durham University, South Road, Durham DH1 3LE, UK

⁴³ Steward Observatory, University of Arizona, 933 North Cherry Avenue, Tucson, AZ 85721-0065, USA

⁴⁴ Department of Physics, Carnegie Mellon University, Pittsburgh, PA 15213

⁴⁵ Center for Astrophysics and Space Astronomy, University of Colorado, 389 UCB, Boulder, CO 80309-0389, USA

⁴⁶ Cerro Tololo Inter-American Observatory/NSF NOIRLab, Casilla 603, La Serena, Chile

Version February 26, 2025

ABSTRACT

We present the Dark Energy Camera All Data Everywhere (DECADE) weak lensing dataset: a catalog of 107 million galaxies observed by the Dark Energy Camera (DECam) in the northern Galactic cap. This catalog was assembled from public DECam data including survey and standard observing programs. These data were consistently processed with the Dark Energy Survey Data Management pipeline as part of the DECADE campaign and serve as the basis of the DECam Local Volume Exploration survey (DELVE) Early Data Release 3 (EDR3). We apply the METACALIBRATION measurement algorithm to generate and calibrate galaxy shapes. After cuts, the resulting cosmology-ready galaxy shape catalog covers a region of $5,412 \text{ deg}^2$ with an effective number density of 4.59 arcmin^{-2} . The coadd images used to derive this data have a median limiting magnitude of $r = 23.6$, $i = 23.2$, and $z = 22.6$, estimated at $S/N = 10$ in a $2''$ aperture. We present a suite of detailed studies to characterize the catalog, measure any residual systematic biases, and verify that the catalog is suitable for cosmology analyses. In parallel, we build an image simulation pipeline to characterize the remaining multiplicative shear bias in this catalog, which we measure to be $m = (-2.454 \pm 0.124) \times 10^{-2}$ for the full sample. Despite the significantly inhomogeneous nature of the data set, due to it being an amalgamation of various observing programs, we find the resulting catalog has sufficient quality to yield competitive cosmological constraints.

1 INTRODUCTION

Measurements of weak gravitational lensing — the deflection of light from distant sources by the intervening matter distribution between the source and the observer — provide important constraints on the growth, evolution, and content of the Universe (Bartelmann & Schneider 2001; Schneider 2005). The cosmological lensing effect, which depends on the gravitational potential field, is seeded by the *total* matter distribution of our Universe. Thus, weak lensing is directly sensitive to *all* matter components, including those that do not emit/absorb light and would otherwise be unobservable. This makes lensing a powerful probe of the underlying structure of the Universe (see Bartelmann & Schneider 2001, for a review of weak gravitational lensing) and of any processes that impact this structure; including modified gravity (*e.g.*, Schmidt 2008), primordial signatures (*e.g.*, Anbajagane et al. 2024c; Goldstein et al. 2024), as well as a wide variety of astrophysical impacts (*e.g.*, Chisari et al. 2018; Schneider et al. 2019; Aricò et al. 2021; Grandis et al. 2024; Bigwood et al. 2024; Anbajagane et al. 2024a).

The primary observable for weak lensing is the *shapes* (or more precisely, the *ellipticities*) of galaxies. Since the first detection of weak lensing more than two decades ago (Bacon et al. 2000; Kaiser et al. 2000; Wittman et al. 2000), the cosmology community has invested significant effort in increasing the statistical power of, and reducing the systematic biases in, these measurements.

At the heart of these advances are increasingly larger and higher-quality datasets, which have consistently grown in sky coverage, depth, and image quality. The community has now evolved from the early weak lensing surveys that have a few million source galaxies¹, such as the Canada-France-Hawaii Telescope Lensing Survey (CFHTLenS, Heymans et al. 2013) and the Deep Lens Survey (DLS, Jee et al. 2013), to current Stage-III² surveys that have tens to a hundred million source galaxies, such as the Kilo-Degree Survey

¹ Throughout this work, we follow common nomenclature used by the community in referring to galaxies used in the weak lensing measurement as “source galaxies”.

² The “Stage-N” terminology was introduced in Albrecht et al. (2006) to describe the different phases of dark energy experiments. There are currently 4 stages, where Stage-III refers to the dark energy experiments that started in the 2010s and Stage-IV refers to those that start in the 2020s.

*dhayaa@uchicago.edu, chihway@kip.uchicago.edu

(KiDS, [de Jong et al. 2015](#)), the Hyper Suprime-Cam Subaru Strategic Program (HSC-SSP, [Aihara et al. 2018](#)), and the Dark Energy Survey (DES, [DES Collaboration et al. 2018](#)). Other datasets, such as the Ultra-violet NearInfrared Optical Northern Survey (UNIONS) are also building source-galaxy catalogs ([Guinot et al. 2022](#)). In the near future, we expect to observe more than a billion source galaxies with the Vera C. Rubin Observatory’s Legacy Survey of Space and Time (LSST, [LSST Science Collaboration et al. 2009](#)). Alongside increases in the statistical power of surveys, there have been significant advances in the methodologies used to measure the shapes of a large number of faint, distant galaxies (e.g., [Bridle et al. 2010](#); [Kitching et al. 2012](#); [Mandelbaum et al. 2015](#)). Currently, shape measurement techniques are reasonably mature and well-understood, but they continue to be improved ([Bernstein & Armstrong 2014](#); [Sheldon et al. 2020](#); [Li & Mandelbaum 2023](#)). These improvements help extract more information from the data and tackle increasingly subtle and complex systematic effects that become more apparent with improvements in statistical precision, data quality, and survey depth.

While we have mentioned many of the current, state-of-the-art lensing surveys above, this list does not encapsulate all of the high-quality *image data* that is currently available for cosmological analyses. In particular, DES has shown that the Dark Energy Camera (DECam, [Flaugher et al. 2015](#)) on the 4-meter Blanco Telescope in Chile is a high-precision system for measuring cosmology from weak lensing. DES used DECam to perform a homogeneous survey covering 5,000 deg² of sky in 760 distinct full- and half-nights from 2013 to 2019 ([DES Collaboration et al. 2021](#)). However, the survey only consists of approximately one-sixth of the data that DECam collected during its nearly continuous operation across more than a decade ([Vivas & Walker 2023](#)).

Here, we present the Dark Energy Camera All Data Everywhere (DECADE) weak lensing dataset, a new shape catalog derived from multi-band DECam imaging in sky area completely outside of the DES footprint. The resulting cosmology-ready sample contains 107 million galaxies assembled from 5,412 deg² of DECam imaging in the northern Galactic cap that does not overlap with DES³. Compared to the shape catalog from the first three years (Y3) of DES data ([Gatti & Sheldon et al. 2021](#)), our new galaxy shape catalog covers $\approx 1,000$ deg² more sky area but with less optimal image quality and uniformity. In particular, DES was designed to optimize the homogeneity of the image depth/quality ([Nielsen et al. 2019](#); [Diehl et al. 2019](#)), while the dataset used in this work is assembled from a wide variety of DECam survey programs and smaller community observations with disparate science

goals. Nonetheless, the exceptional field of view and image quality of DECam, coupled with the large collecting area of the 4-meter Blanco Telescope, make the DECADE shape catalog a powerful dataset for cosmology. In particular, our catalog has three million more galaxies than the one from DES Y3 ([Gatti & Sheldon et al. 2021](#)) and as a result the two datasets have similar statistical power.

In order to confidently leverage the DECam data for weak lensing analysis, we apply mature and well-vetted pipelines for data reduction and shape measurement to the imaging data. We process the community DECam data with the DES Data Management (DESDM) pipeline ([Morganson et al. 2018](#)) at the National Center for Supercomputing Applications (NCSA) as part of the DECADE data processing campaign. This includes the full complexity of the calibration products and algorithms developed by the DES Collaboration to correct for instrumental effects ([Gruen et al. 2015](#); [Bernstein et al. 2017b, 2018](#); [Morganson et al. 2018](#)). Following DES Y3, we apply the well-characterized METACALIBRATION shear measurement algorithms ([Sheldon & Huff 2017](#); [Huff & Mandelbaum 2017](#)) to measure shapes of the detected sources. Wherever possible, we follow the analysis procedures and validation processes developed for the DES cosmology analysis. As such, our catalog and subsequent shear analysis present a novel cross check on the DES cosmic shear cosmology analysis as we apply very similar algorithms and analysis choices to a completely independent catalog of comparable statistical precision.

The DECADE shape catalog has some unique features that make it especially valuable given the recent trends seen in weak lensing datasets, where the measurement of the cosmological parameter σ_8 (defined as the normalization of the matter fluctuations on $8h^{-1}$ Mpc scales) is systematically low compared to that from the CMB data ([Asgari et al. 2021](#); [Amon et al. 2022](#); [Secco & Samuroff et al. 2022](#); [Dalal et al. 2023](#)). Primarily, a majority of our data covers a region of the sky that has no overlap with other Stage-III lensing surveys and thus provides an important, independent statistical sample for measuring σ_8 .

In addition, our data will be fairly compatible with the DES data (given the similarity in the processing pipeline and other analysis choices), making it easier to compare to, and combine with, the lensing cosmology constraints from DES (following e.g., [Chang et al. 2019](#); [Longley et al. 2023](#); [DES & KiDS Collaborations et al. 2023](#)). Finally, our data covers a region of the sky that has significant overlap with large spectroscopic surveys such the Sloan Digital Sky Survey ([York et al. 2000](#)) and the Dark Energy Spectroscopic Instrument ([DESI Collaboration et al. 2016](#)), as well as ground-based CMB experiments such as the South Pole Telescope ([Carlstrom et al. 2011](#)), the Atacama Cosmology Telescope ([Fowler et al. 2007](#);

³ All areas in this paper are calculated using a HEALPIX map ([Górski et al. 2005](#)) of NSIDE=4096, with a binary mask (the full pixel area is counted as long as there is one galaxy in that pixel).

Thornton et al. 2016), and the Simons Observatory (Ade et al. 2019). This overlap allows for important systematic checks on photometric redshifts (e.g., Schneider et al. 2006; Newman 2008; Ménard et al. 2013; Cawthon et al. 2022; Giannini et al. 2022), intrinsic alignment models (e.g., Samuroff et al. 2023) as well as for opportunities in cross-correlation analyses for a variety of different science cases (e.g., Vikram et al. 2017; Omori et al. 2019; Shin et al. 2019; Pandey et al. 2019; Chang et al. 2023; Sánchez et al. 2022; Anbajagane et al. 2024b; Bocquet et al. 2024).

Throughout this paper, we closely follow the analysis choices and methodology used to assemble and test the DES Year 1 (Y1) and Year 3 (Y3) shape catalogs, as described in Zuntz & Sheldon et al. (2018) and Gatti & Sheldon et al. (2021, hereafter *GS21*), respectively. This paper is the first in a series of four papers describing the DECADE cosmic shear analysis. This paper (hereafter *PAPER I*) describes the shape measurement method, the final cosmology sample, and the robustness tests and image simulation pipeline from which we quantify the accuracy of the shear measurements. The second paper (Anbajagane et al. 2025a, hereafter *PAPER II*) describes the tomographic bin selections and calibrated redshift distributions for our cosmology sample (including the synthetic source injection pipeline needed for these tasks) alongside a series of validation tests of the redshift distributions. The third paper (Anbajagane & Chang et al. 2025b, hereafter *PAPER III*) defines the modeling choices of the cosmology analysis — including scale cuts, blinding strategy, covariance validation etc. — as well as the robustness of our cosmology analysis against a variety of systematics, including the point spread function (PSF) contamination, survey inhomogeneity etc. Finally, the fourth paper (Anbajagane & Chang et al. 2025c, hereafter *PAPER IV*) performs the cosmological inference with our cosmic shear measurements.

This paper is structured as follows. In Section 2, we briefly describe the processing of the DECam data and detail the construction of the base galaxy catalog. In Section 3, we introduce the METACALIBRATION algorithm used for the shear estimation, the different selection cuts we apply, and the characteristics of the resulting galaxy shape catalog. In Section 4, we analyze the catalog to quantify any residual systematic uncertainties in our measurements and validate these measurements through a series of null-tests. In Section 5, we describe the image simulation pipeline used to quantify the residual shear calibration bias in our catalog. We summarize in Section 6.

2 DATA PROCESSING

2.1 DELVE Early Data Release 3

The data used here were assembled from public DECam data available by December 2022. The largest contributing programs are the DECam Legacy Survey (DECaLS, Dey et al. 2019), DECam Local Volume Exploration survey (DELVE, Drlica-Wagner et al. 2021, 2022), and the DECam eROSITA Survey (DeROSITAS, PI: Zenteno). When combined with other community observations, the public DECam data cover more than 21,000 deg² of the high Galactic latitude ($|b| > 10^\circ$) sky (Drlica-Wagner et al. 2022). The data products described here were produced for the DELVE Early Data Release 3 (DELVE EDR3), which is a consistent reduction of the public archival DECam data using the DESDM software pipeline (Morganson et al. 2018) and was carried out as part of the DECADE data processing campaign mentioned previously. The primary advance in DELVE EDR3 relative to previous DELVE data releases is the generation of coadd images and catalogs, as well as multi-epoch data products and object fits that serve as the basis of high-quality shape measurements discussed here. The processing of individual DECam images, the coaddition of multiple DECam images, the detection of sources, and the measurement of their properties follow similar configurations to DES Data Release 2 (DES DR2, DES Collaboration et al. 2021) and DES Y6 (Bechtol et al. 2025). The DELVE EDR3 processing is also briefly described in Tan et al. (2024).

The DELVE EDR3 data set is assembled from the region of the north Galactic cap that is observable by DECam. We select exposures that pass a set of quality criteria that are described in Tan et al. (2024) and are also summarized below:

- Located in the northern Galactic cap, defined with Galactic latitude $b > 10^\circ$. The data contain images at sky-locations up to Dec. $\leq 33^\circ$, a limit imposed by the location of the Blanco telescope in the Southern Hemisphere,
- Exposure time between $30 \leq t_{\text{exp}} \leq 350$ seconds, since the DESDM processing pipeline has not been extensively tested for coadding images with a broader range of exposure times,
- PSF full-width half-max (FWHM) of $0'' < \text{FWHM} < 1.5''$,
- Good image quality (see Tan et al. 2024) in addition to $t_{\text{eff}} > 0.2$, where t_{eff} is a summary of the exposure quality (Neilsen et al. 2016),
- Good astrometric solutions, determined via comparisons with *Gaia* DR2. See Section 2 in Tan et al. (2024) for the precise comparison criteria,

- Number of objects detected in each exposure is $< 7.5 \times 10^5$, to remove exposures with many spurious object detections caused by excessive electronic noise or poor background subtraction,
- Images are further checked for quality by automated algorithms and human visual inspection.

This results in 42,700 exposures across the *griz* bands (Tan et al. 2024). With these exposures, we produce the multi-epoch coadded images (Morganson et al. 2018), SOURCEEXTRACTOR (Bertin & Arnouts 1996) source detection catalogs, multi-epoch data files (MEDs; Jarvis et al. 2016), and catalogs with the multi-epoch, multi-object fits (e.g., Sheldon 2014; Drlica-Wagner et al. 2018). In particular, we use the $r + i + z$ coadd images for object detection. The *g* band is not used for detection, or for any downstream postprocessing such as shear measurement or redshift estimation, as is the case with DES Y3. The image coadds are produced in distinct rectangular tiles that have dimensions of $0.71^\circ \times 0.71^\circ$, where each dimension is covered by 10,000 pixels with a pixel scale of $0.263''$. A coadd tile is built and processed only if it has at least one exposure in each of the four bands (*griz*) intersecting that region on the sky. The EDR3 region contains 16,895 coadd tiles covering a total area of $\approx 8,500 \text{ deg}^2$. Note that this is prior to all additional selections needed to assemble the cosmology-ready galaxy sample. The latter covers $5,412 \text{ deg}^2$ as mentioned previously.

In the DESDM processing pipeline (Morganson et al. 2018), a PSF model is fit to each individual CCD image using PSFEX (Bertin 2013) prior to image coaddition. These models are used in all object fits provided in the general-purpose DES “Gold” catalogs (Drlica-Wagner et al. 2018; Sevilla-Noarbe et al. 2021; Bechtol et al. 2025). These models were also used for weak lensing analyses in the DES Science Verification (SV) and Y1 datasets (Jarvis et al. 2016; Zuntz & Sheldon et al. 2018) and also in other surveys such as KiDS (Giblin et al. 2021). However, more recent lensing analyses from DES Y3 and Y6 (GS21, Yamamoto & Becker et al. 2025) fit and use a different PSF model constructed via the “PSFs in the Full Field-of-View” software (PIFF, Jarvis et al. 2020). In DES Y3 and Y6, the PIFF models are generated in addition to the PSFEX ones, via a dedicated post-processing step. In DECADE, we did not have the resources to post-process all single-epoch CCD images to generate PIFF solutions for the image PSFs. Therefore, PSFEX serves as our PSF model.

The use of PSFEX rather than PIFF introduces several differences in our PSF modeling compared to the latest DES Y6 models (Schutt et al. 2025). The most important of these differences between PSFEX and PIFF are that the former uses a different star selection criteria compared to the latter, and the former also does not have any color-dependent modeling as

present in the latter. Though, we note that the DES Y3 shape catalog (GS21) used a color-independent PSF model from PIFF for its shape measurements. Additionally, PIFF models the PSF in sky coordinates, rather than image coordinates, which helps alleviate (but not remove) the impact of “tree rings” in the PSF solutions; see Figure 5 and discussions therein. The systematic diagnostic tests in Section 4 characterize our PSF model and show it has a small impact on the lensing data vector, while PAPER III explicitly confirms that the final cosmological results are insensitive to any residual, additive contaminations from the PSF. Details of the PSFEX model choices are recorded in Appendix A.

2.2 Base catalog selection

Analogous to the “Gold catalog” in DES (Drlica-Wagner et al. 2018; Sevilla-Noarbe et al. 2021; Bechtol et al. 2025), we define a “base catalog” that serves as a starting point for any cosmology analysis on this data. This is obtained by performing the following selection cuts on the SOURCEEXTRACTOR catalog generated from the coadded images:

- **SOURCEEXTRACTOR flags.** We select objects according to the following SOURCEEXTRACTOR flags: `FLAGS_[GRIZ]<=3, IMAFLAGS_ISO_[GRIZ]==0`. This cut removes any objects that are clear artifacts.
- **FITVD flags.** All SOURCEEXTRACTOR objects are processed through the FITVD⁴ pipeline (Bechtol et al. 2025), which jointly fits all exposure-level cutouts of the object in all bands. We remove any objects that have failed FITVD measurements.
- **Foreground masking.** Following DES Y3, we mask a number of regions in the survey footprint. First we cutout circles around bright sources:
 - Stars from 2MASS (Skrutskie et al. 2006),
 - Stars from *Gaia* eDR3 (Gaia Collaboration et al. 2021),
 - The Yale bright star catalog (Hoffleit & Jaschek 1991),
 - A list of very bright stars from the BSCP5 catalog⁵ (Hoffleit, D. & Warren Jr, W. H. 1991),
 - Galaxies from the Hyperleda catalog⁶ (Makarov et al. 2014)
 - Globular clusters from the Harris catalog (Harris 1997, 2010 edition)

We additionally remove areas of the sky with high stellar

⁴ <https://github.com/esheldon/fitvd>

⁵ These bright stars, some of which will also be included in the aforementioned catalogs, are masked separately from the rest. Their brightness necessitates larger masks because these sources cause scattered light artifacts in the DECam images.

⁶ <http://leda.univ-lyon1.fr/>

density, defined by the number density of *Gaia* objects (with $G < 21$ mag) exceeding 5 arcmin^2 , and also areas with high interstellar extinction, defined by $E(B - V) > 0.2$ according to the extinction map of [Schlegel et al. \(1998\)](#). These cuts ensure that the stellar density and dust extinction in the EDR3 footprint have a similar maximum bound as seen in the DES Y3 region of the sky. The final foreground mask removes roughly 30% of objects and about $2,000 \text{ deg}^2$.

- **Other masks.** We finally remove a small number of objects in regions that either have a statistically significant surplus of unphysical colors⁷ (indicating failures in zeropoint calibration or astrometry) or are located in areas that are very disjoint from the main contiguous footprint. This removes $< 1\%$ of objects that pass all the other cuts above.

After all cuts above, we are left with 470,812,637 objects covering an area of $\approx 5750 \text{ deg}^2$. While we broadly follow the procedure used in DES Y3 ([Sevilla-Noarbe et al. 2021](#)), we do not include flag bit 32 and 64 from their Table 3, which correspond to bright blue artifacts in the images and bright objects with unphysical colors, respectively. These objects are extremely rare — they constituted $< 0.3\%$ of the base catalog in DES Y3 ([Sevilla-Noarbe et al. 2021](#), see their Table 3) — and most do not survive our shape catalog selection described in the next section. For example, the DES Y3 color cuts corresponding to flag bit 64, which are defined as $-1 < X < 4$ with $X = a - b$ being the magnitudes in two different bands, are nearly the same as the color cuts placed on the galaxy shape catalog (see Section 3.2). We verified, using the DES Y3 catalog and flags, that such bright objects and unphysical color objects only constitute 0.01% and 0.003% of the catalog after the sample selection defined above.

2.3 Differences relative to DES

The image processing used in deriving the DECADE shape catalog is heavily based on that of DES. However, there are three areas where our dataset and processing *differ* from DES Y3, which we describe below for reference.

Survey inhomogeneity. DES observed $5,000 \text{ deg}^2$ of the sky with ten 90-second exposures in *griz* and an equivalent depth of ten 45-second exposures in *Y*. It used real-time data quality assessments to guide observing decisions (*i.e.*, telescope time during poor observing conditions was allocated to supernova observations; [Neilsen et al. 2019](#)). Our data,

⁷ These objects are defined with $\text{SNR} > 10$, and having colors *outside* the range $-1 < X < 4$ for any of the colors $X \in \{g - r, r - i, i - z\}$. We then identify regions of the sky (partitioned into HEALPIX pixels of $\text{NSIDE} = 256$) with at least 10 selected objects and mask the area in these pixels. This cut is separate from the colors cuts presented in Section 3, where the latter are motivated by details in the redshift estimation procedure.

on the other hand, is significantly less homogeneous. The DECam survey programs covering large areas of the sky each followed a variety of strategies for optimizing homogeneity (e.g., [Dey et al. 2019](#); [Drlica-Wagner et al. 2021](#)), while the presence of additional survey and standard programs covering smaller fractions of the sky necessarily lead to additional inhomogeneity in our final dataset. We refer readers to [Tan et al. \(2024\)](#) for a description of the exposure selection process used to reduce some of these inhomogeneities prior to image processing.

Airmass distribution. The DECam optics were not designed to remove differential chromatic refraction (DCR) from the atmosphere (e.g., [Bernstein et al. 2017a](#), see their Section 4.7). For this reason, the DES wide-area footprint and corresponding observing strategy are defined to have an airmass of $\sec(z) \leq 1.4$, where z is the zenith angle. The northern Galactic cap surveyed in this work naturally extends to higher airmass — 25% of our catalog objects are in regions with $\sec(z) > 1.4$ and 4% are in regions with $\sec(z) > 1.8$ — which then results in a residual point spread function (PSF) modeling error due to DCR.⁸ We do not detect a significant correlation between measured shear and DCR as a result of this effect (see Section 4.7 and the tests in [PAPER III](#)).

PSF model. As mentioned previously, the PSF model algorithm used for shape measurements in this catalog, PSFEX ([Bertin 2013](#)), is different from the PIFF ([Jarvis et al. 2020](#)) algorithm used in the most recent DES lensing analyses ([GS21](#), [Yamamoto & Becker et al. 2025](#)). We extensively test the impact of the different PSF model used in our work and find no significant impact of the PSF systematics on the shape catalog (see Section 4 and also the tests in [PAPER III](#)). We provide additional details on our PSF modeling approach, and on its differences from the DES Y3/Y6 analysis choices, in [Appendix A](#).

These differences between DECADE and DES provide us with the opportunity to study the limits on image/data quality at which various algorithms still function without introducing substantial systematic biases. These results could have implications for the next generation of datasets, such as LSST, where a significant amount of additional image data could be incorporated into the analyses if we are able to extend lensing datasets to regions with higher airmass and less homogeneous coverage. See [Bianco et al. \(2022\)](#) for an example of the proposed LSST footprint.

⁸ The PSF size and ellipticity are color-dependent due to the DCR effect. Across the wavelength range spanned by each filter band, stars and galaxies can have slightly different spectral energy distributions (SEDs); stars are usually bluer than galaxies. Thus, when we use stars to build a PSF model and apply the model to galaxies when estimating shapes, we introduce a small error that is associated both with the difference in the SED of stars and galaxies, and with the amplitude of the DCR effect. This amplitude is greater at high airmass.

3 SHAPE CATALOG

A weak lensing analysis requires estimating some tracer of the lensing shear field, often taken to be the galaxy shapes. Typically, we use measurements of the two-component ellipticity \mathbf{e} , with $\mathbf{e} = e_1 + ie_2$. Various methods have been used to measure these ellipticities, though a precise measurement is made challenging due to the presence of noise, pixel masks, the PSF, selection effects, etc. of our observations. In the presence of external cosmological shear $\boldsymbol{\gamma} = \gamma_1 + i\gamma_2$, the observed ellipticities change, and the resulting change in a particular shape estimate defines the *response*, typically denoted R . In the case when \mathbf{e} is the shape estimate, we can schematically write $R = \delta\mathbf{e}/\delta\boldsymbol{\gamma}$. Having an unbiased measure of R is essential to achieving unbiased cosmological constraints. Over the past decade, there has been a rich literature devoted to developing algorithms that can robustly measure R , a process sometimes referred to as “shear calibration” (see e.g., Mandelbaum 2018, for an overview of the various methods). Of these, we use the METACALIBRATION algorithm (Sheldon & Huff 2017; Huff & Mandelbaum 2017). In this work, all shear-related estimates are performed using image data from only the *riz* bands; we discard the *g*-band data, following the DES Y3 findings of significant PSF modelling uncertainties in that band (Jarvis et al. 2020).

3.1 METACALIBRATION

METACALIBRATION (Sheldon & Huff 2017; Huff & Mandelbaum 2017) is a shear calibration method and is the fiducial method used in GS21. We refer the reader to the original papers for details of the method. Here we only sketch the conceptual idea behind the method and introduce the equations that we will refer to later in this work.

The key idea of METACALIBRATION is that we can estimate the response, R , by artificially shearing the data at the pixel level. Particularly, for each galaxy, the method requires five versions of the same image: (no shear, 1+, 1−, 2+, 2−). Aside from the “no shear” version, which is the original, the other four are obtained by shearing the images by a small amount ($\Delta\gamma_{i\pm} = \pm 0.01$, $i = 1, 2$) positively/negatively in the two sky coordinates 1 and 2. The same shape measurement code is run on all five versions of the image cutouts of this galaxy, resulting in five versions of the galaxy’s ellipticity measurement. In this work, our shape measurements are based on NGMIX (Sheldon 2014) and fit galaxy images using an elliptical Gaussian convolved with the PSF model. In addition to the ellipticities, we also measure all the other object properties (such as photometry) in all five variants associated with the galaxy.

We can now calculate two response factors from the five measurements detailed above. The first response factor \mathbf{R}_γ

is the response of the ellipticity estimate to external shear, as discussed earlier, and it can be calculated via

$$[\mathbf{R}_\gamma]_{ij} = \frac{e_i^{j+} - e_i^{j-}}{2 \times 0.01}; \quad i, j = 1, 2. \quad (1)$$

We note that \mathbf{R}_γ can be calculated for every galaxy; though for a single galaxy the estimate is generally dominated by noise. When calibrating summary statistics used for cosmological inference, we follow DES analyses and only use the average response of the relevant sample, in which case the response estimate is no longer noisy.

The second response factor, denoted \mathbf{R}_S , is related to how external shear also affects the selection of the galaxy sample (Sheldon & Huff 2017, see their Equations 12-14). This is because objects can pass/fail a given selection when sheared. “Selection” here refers to the cuts we place on the sample, using quantities such as galaxy size and signal-to-noise. We discuss the full list of selections in Section 3.2. This selection response is calculated using the five versions of the shape measurements. In particular, we perform the same selection using the $i+$ and $i-$ versions of e.g., galaxy size, signal-to-noise, and any other METACALIBRATION quantity used in the selection function. The selection response is then

$$\langle \mathbf{R}_S \rangle_{ij} \approx \frac{\langle e_i \rangle^{S_{i+}} - \langle e_i \rangle^{S_{i-}}}{\Delta\gamma_j}, \quad (2)$$

where S denotes the full set of selections applied to the catalogs, and S_{i+} denotes that the selections were performed using measurements from the $i+$ sheared images as extracted from METACALIBRATION. Note that \mathbf{R}_S can only be calculated for an ensemble since the selection effect is fundamentally a response of the sample; the selection S_{i+} and S_{i-} is not guaranteed to return the same galaxies, and that is precisely the effect being calibrated. We briefly mention that the DES Y6 catalog (Yamamoto & Becker et al. 2025) uses the METADETECTION algorithm (Sheldon et al. 2020), which also accounts for a detection-based response in addition to the terms above (since detection is also formally part of the selection term). For this work, which uses METACALIBRATION-based estimates, we follow DES Y3 in calibrating such detection-based effects using suites of image simulations, as undertaken in DES Y3 MacCrann & Becker et al. (2022) and described in Section 5 below.

Finally, the full response factor for a sample of galaxies is the sum of the two response factors above, or

$$\langle \mathbf{R} \rangle = \langle \mathbf{R}_\gamma \rangle + \langle \mathbf{R}_S \rangle. \quad (3)$$

In practice, we take the $\langle \mathbf{R} \rangle$ matrix to be diagonal, since the off-diagonal terms are negligible, and also take the mean of the two diagonal elements as the single response factor when performing the cosmic shear measurements. Our implementation, including all assumptions therein, exactly follow the procedure verified and chosen in GS21.

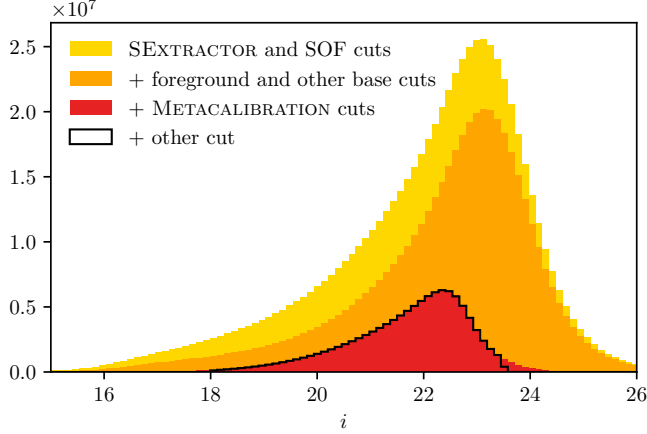


Figure 1. The i band magnitude distribution as a function of different selection cuts applied to derive the final shape catalog. The size of the final sample (black) is approximately 16% the size of the sample with only SOURCEEXTRACTOR and FITVD cuts (gold).

3.2 Shear sample selection

Starting from the raw catalog containing all SOURCEEXTRACTOR detections, we closely follow GS21 and place the following selection cuts to form the final shape catalog:

- The base selection described in Section 2.2
- Have a corresponding measurement in the METACALIBRATION catalog⁹ and pass the METACALIBRATION cuts,

$$\begin{aligned}
 &10 < \text{SNR} < 1000; \\
 &T/T_{\text{psf}} > 0.5; \\
 &T < 10; \\
 &\text{NOT}((T > 2) \text{ and } (\text{SNR} < 30)). \quad (4)
 \end{aligned}$$

Here T and SNR are the size (in arcsec²) and signal-to-noise estimates for the galaxy, whereas T_{psf} is the size estimate of the PSF. All these quantities are outputs from METACALIBRATION.

- Remove galaxies that (i) are very faint/bright in either of the three bands, and (ii) exhibit extreme colors that are unexpected for a galaxy sample, as both considerations help improve the photometric redshift uncertainties and calibration of the catalog (Myles & Alarcon et al. 2021,

⁹ Not every SOURCEEXTRACTOR detection has a METACALIBRATION measurement, as the latter explicitly removes any galaxy for which we do not have simultaneous coverage across the riz bands. Thus, this selection implicitly contains such a cut as well.

see their Section 3.1)

$$\begin{aligned}
 &15 < r < 26 \\
 &18 < i < 23.5 \\
 &15 < z < 26 \\
 &-1.5 < r - i < 4 \\
 &-1.5 < i - z < 4. \quad (5)
 \end{aligned}$$

- Remove binary stars (or close stellar pairs), which can appear as highly elliptical sources due to blending and due to limited resolution in our images. These are discarded by selecting all objects with $\sqrt{e_1^2 + e_2^2} > 0.8$, and then removing those with

$$\log_{10}\left(\frac{T}{\text{arcsec}^2}\right) > \frac{22.25 - r}{3.5}. \quad (6)$$

This cut was motivated by visual checks on the DES Y3 data (GS21). We have verified the presence of these objects in our catalog as well and therefore replicate these cuts in our analysis.

- Finally, when performing a tomographic cosmic shear analysis, we place these galaxies into tomographic bins according to their redshift estimates. We define four tomographic bins roughly in the redshift range of $0 < z < 2$ (see details in PAPER II). Note that no galaxies are discarded during this selection.

All magnitudes in the above selection use METACALIBRATION fluxes rather than the fluxes estimated by the FITVD model fit described in Section 2.2 – the use of the former photometry is required to accurately employ the METACALIBRATION response formula (Equation 2) and derive the selection bias. All color/magnitude cuts are made on *de-reddened* photometric estimates, where the de-reddening correction $A_b \times E(B - V)$ in band b uses the $E(B - V)$ map of Schlegel et al. (1998) with the filter-dependent factors A_b as calculated and presented in DES DR1 (DES Collaboration et al. 2018, see their Section 4.2). The reddening coefficients are 2.140, 1.569, 1.196 for the riz bands.

The final selection function results in a catalog of 107,371,478 galaxies, covering 5,412 deg² of the sky. Figure 1 and Table 1 show the changes in the sample size as a function of the different cuts. Figure 2 shows the number density of the galaxies in the final shape catalog and also plots footprints from other external datasets for comparison. The number density of our catalog is generally higher in the center of the footprint and lower on the eastern/western edges (where stellar density increases due to proximity to the Galactic plane), and some fluctuations in this number density exhibit sizes corresponding to the DECam focal plane. The latter fluctuations are almost exclusively in regions that are deeper than the median depth of

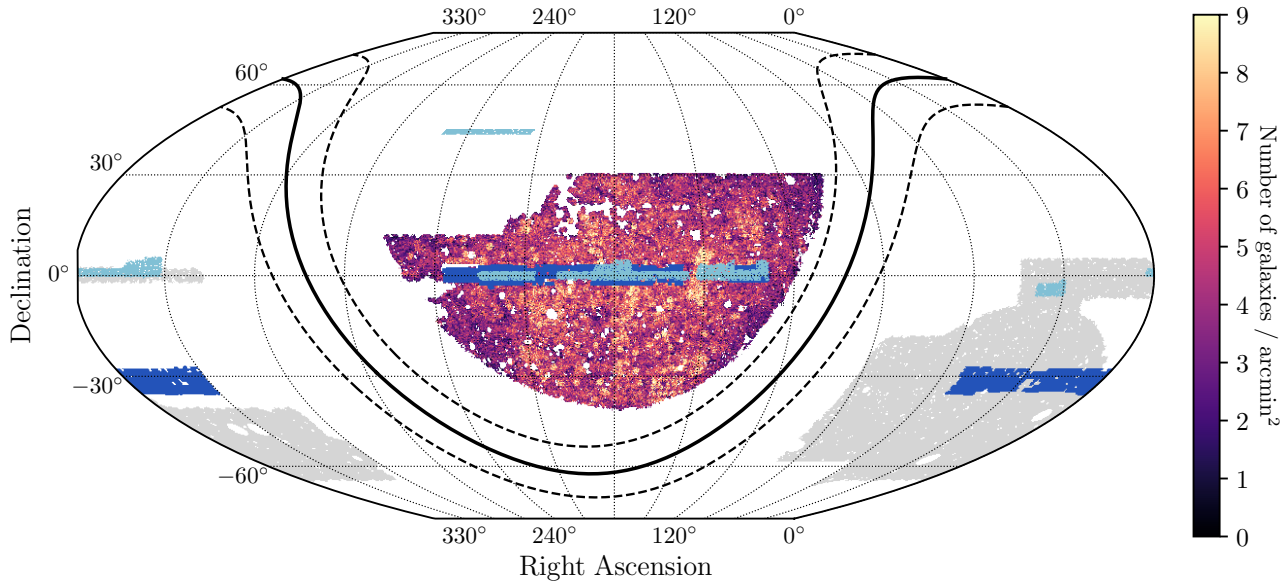


Figure 2. Map of the number density of galaxies in our shape catalog. We also show the footprint of three other Stage-III lensing surveys: DES Y3 (grey), KiDS-1000 (dark blue), HSC Y3 (light blue). The dashed lines indicating the Galactic plane with $b = \pm 10^\circ$. Our catalog consists of 107 million galaxies covering an area of $5,412 \text{ deg}^2$. The distance between our footprint and the Galactic plane is a result of our stellar density mask. This mask is also asymmetric due to the presence of the Galactic bulge.

the DECADE data (see Figure 12). This is expected given the origin of our dataset, which is an amalgamation of community DECam data used for various science goals. In PAPER III (see their Section 6), we perform numerous tests that indicate the impact of such variations on our cosmology constraints is below the precision of the dataset.

In order to make a direct comparison between the imaging data of the DECADE and DES datasets, we show the 10σ limiting magnitude for photometry computed with $2''$ apertures. Figure 3 shows the distribution of these limiting magnitudes over the footprint spanned by our shape catalog and that by the DES Y3 sample. The median limiting magnitude of our data in each band is $r = 23.6$, $i = 23.2$, $z = 22.6$. These numbers can be directly compared with the “Median Coadd Magnitude Limit” in Table 2 of Sevilla-Noarbe et al. (2021), where they find $r = 24.0$, $i = 23.3$, $z = 22.6$ – our imaging data is slightly shallower than DES Y3 in r, i , and similar to it in z . The image depth varies significantly more in DECADE than DES Y3, as is expected. In fact, around 10% of the DECADE footprint is *deeper* than the 99% value found in the DES Y3 distribution. We stress, however, that this only characterizes the image depth and not number density of the source galaxy catalog. Figure 1 in PAPER III shows that the spatial variations in our source galaxy number density have a *similar amplitude* to that seen in DES Y3. The magnitude cuts in the selection function described above, which were motivated by redshift precision considerations, reduce inhomogeneities in the source galaxy number density (as caused by the inhomogeneous image

Selection type	Number (%)	Cumulative number (%)
SrcEXT + FITVD	671,290,620 (100%)	671,290,620 (100%)
Foreground + base	470,812,637 (70.14%)	470,812,637 (70.14%)
METACALIBRATION	140,432,055 (20.92%)	111,400,589 (16.59%)
Other	480,429,730 (71.57%)	107,371,478 (15.99%)

Table 1. Number of galaxies as a function of the different selection cuts applied to form the shape catalog. The first column shows the number of galaxies (and percentage relative to the first row) that pass a single type of cut, while the second column shows the cumulative numbers from combining the cuts sequentially, where the sequence is ordered from top to bottom.

depth/quality).

3.3 Weights

In this work, each galaxy is assigned a weight that optimizes the signal-to-noise of statistics computed with the galaxy shapes. That is, galaxies with noisier shear measurements will be down-weighted and vice versa. Following GS21, the weight of each galaxy is assigned according to their signal-to-noise¹⁰ and size, as estimated in METACALIBRATION. We first calculate two quantities $(\sigma_e^2)_{jk}$, $\langle R \rangle_{jk}$ for galaxies binned into size ratio bin j and signal-to-noise bin k . Here, the size ratio is the size of the galaxy to the

¹⁰ For clarity, we reproduce footnote 8 from GS21 on the definition of this signal-to-noise: “we define the signal-to-noise ratio (S/N) as $S/N = (\sum_p m_p I_p / \sigma_p^2) / (\sum_p m_p^2 / \sigma_p^2)^{1/2}$ where the sum runs over the pixel p , m_p is the best fit model for the galaxy, I_p the measured pixel value, and σ_p the estimated pixel variance.”

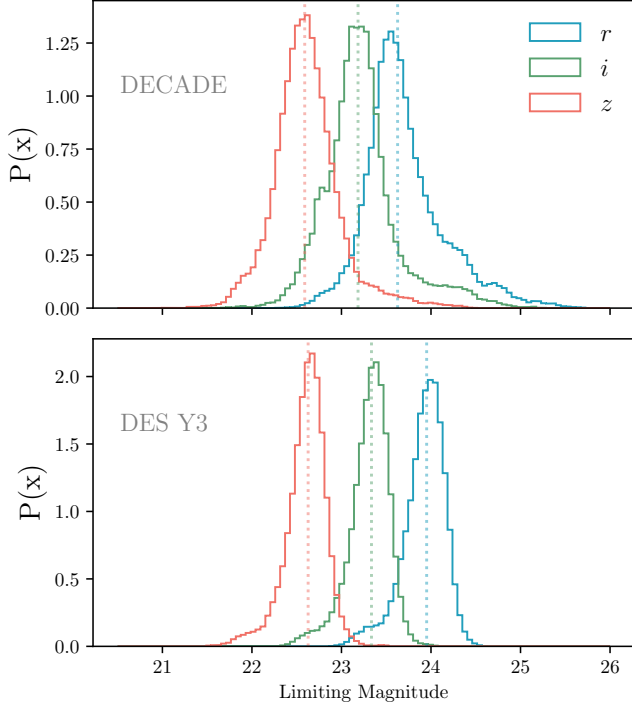


Figure 3. Distribution of the limiting magnitude in the riz bands across the footprint for our shape catalog (top) and the DES Y3 catalog (bottom). The median limiting magnitudes, shown as vertical dotted lines, are $r = 23.63(23.95)$, $i = 23.18(23.34)$, and $z = 22.59(22.63)$ for DECADE (DES). The DECADE data has a similar median magnitude as DES Y3, but a considerably wider spread. Around 10% of our area has a higher magnitude limit than the 99% maximum value in DES Y3 (for each band). This map only shows spatial variations in the imaging data quality, and not in the source-galaxy number densities, which is cut at brighter magnitudes and therefore shows less variation (see Figure 1 in PAPER III).

PSF, (T/T_{PSF}) . Following GS21, we choose 20 logarithmic bins in size ratio from $0.5 < (T/T_{\text{PSF}}) < 5$ and 20 logarithmic bins in signal-to-noise from $10 < \text{SNR} < 330$. This range includes 97.5% of all the source galaxies. Remaining galaxies with large SNR or (T/T_{PSF}) are subsumed into the last bin of the respective quantity.

The quantity $(\sigma_e^2)_{jk}$ is the variance in the single-component ellipticity within a cell jk of the 2D grid, defined as

$$(\sigma_e^2)_{jk} = \frac{1}{2N_{jk}} \sum_i^{N_{jk}} (e_{1,i}^2 + e_{2,i}^2), \quad (7)$$

where N_{jk} is the number of galaxies in bin jk , while e_1 and e_2 are the single-component, uncalibrated ellipticities from galaxies in bin jk . $\langle R \rangle_{jk}$ is the mean, unweighted shear response in bin jk as calculated using Equation 3.

Each bin is then assigned the weight

$$w_{jk} = \frac{\langle R \rangle_{jk}^2}{(\sigma_e^2)_{jk}} \quad (8)$$

and all galaxies in cell jk are assigned weight w_{jk} . For galaxies with sizes and/or signal-to-noise values outside the grid defined above, we assign weights corresponding to the closest grid point. Figure 4 shows the number counts, σ_e^2 , $\langle R \rangle$ and w , as a function of size ratio and signal-to-noise. Compared with Figure 4 of GS21, we see fairly similar patterns in the number counts, $\langle R \rangle$ and weights. There are some minor difference in the shape noise distribution, but these are *a priori* expected due to the difference in image quality between our data and DES Y3. Thus, they are not signs of any underlying issue in our data.

3.4 Response, number counts and shape noise

Given the weights described above, we can estimate the effective number density of source galaxies, n_{eff} , as well as the associated shape noise, σ_e , of our sample. These numbers, together with the area of our footprint A , provide a first-order estimate for the statistical power of this dataset. Following previous work, we calculate two versions of n_{eff} and σ_e based on Heymans et al. (2012) and Chang et al. (2013) for easy comparison with other datasets.

First, following Heymans et al. (2012), we define

$$n_{\text{eff,H12}} = \frac{1}{A} \frac{(\sum w_i)^2}{\sum w_i^2} \quad (9)$$

$$\sigma_{e,\text{H12}}^2 = \frac{1}{2} \left[\frac{\sum (w_i e_{1,i})^2}{(\sum w_i)^2} + \frac{\sum (w_i e_{2,i})^2}{(\sum w_i)^2} \right] \left[\frac{(\sum w_i)^2}{\sum w_i^2} \right] \quad (10)$$

Second, following Chang et al. (2013), we define

$$n_{\text{eff,C13}} = \frac{1}{A} \frac{\sigma_{e,\text{C13}}^2 (\sum w_i R)^2}{\sum w_i^2 \left(R^2 \sigma_{e,\text{C13}}^2 + \frac{1}{2} (\sigma_{m,1,i}^2 + \sigma_{m,2,i}^2) \right)} \quad (11)$$

$$\sigma_{e,\text{C13}}^2 = \frac{1}{2} \frac{\sum w_i^2 (e_{1,i}^2 + e_{2,i}^2 - \sigma_{m,1,i}^2 - \sigma_{m,2,i}^2)}{\sum w_i^2 R^2}, \quad (12)$$

where $\sigma_{m,1,i}^2$ and $\sigma_{m,2,i}^2$ are the measurement noise estimated via METACALIBRATION.

Table 2 summarizes the final n_{eff} and σ_e values for the two definitions and for both the full sample and also the sample split in four tomographic bins. In PAPER III and PAPER IV, we show that the DECADE shape catalog has similar

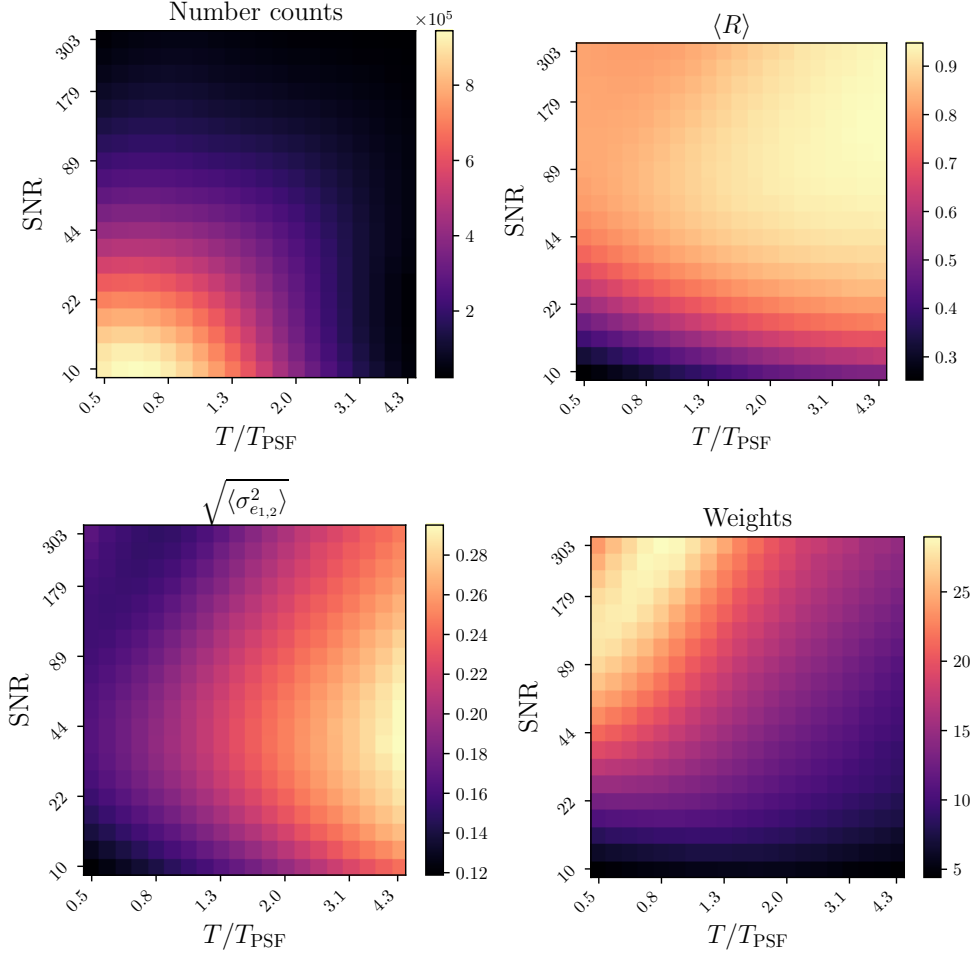


Figure 4. Number counts (upper left), shear response $\langle R \rangle$ (upper right), shape noise $\sqrt{\langle \sigma_{\epsilon}^2 \rangle}$ (lower left) and shear weights (lower right) as a function of size ratio (T/T_{PSF}) and signal-to-noise (SNR) of the galaxy. For each galaxy in the final shape catalog, a weight is assigned according to the lower right panel. Including this weight enhances the signal-to-noise of any statistic computed with the shape catalog.

	n	$R_{\gamma,1}$	$R_{S,1}$	$R_{\text{tot},1}$	$R_{\gamma,2}$	$R_{S,2}$	$R_{\text{tot},2}$	$n_{\text{eff,C13}}$	$\sigma_{e,\text{C13}}$	$n_{\text{eff,H12}}$	$\sigma_{e,\text{H12}}$	$\langle \gamma_1 \rangle$	$\langle \gamma_2 \rangle$
Bin 1	1.396	0.850	-0.014	0.836	0.851	-0.014	0.837	1.229	0.232	1.239	0.233	0.00012	-0.00059
Bin 2	1.371	0.761	0.009	0.771	0.762	0.009	0.771	1.130	0.257	1.150	0.259	0.00026	-0.00078
Bin 3	1.375	0.721	0.018	0.740	0.722	0.020	0.742	1.134	0.244	1.169	0.248	0.00026	-0.00090
Bin 4	1.369	0.592	0.028	0.620	0.593	0.028	0.621	1.054	0.276	1.153	0.289	0.00051	-0.00108
Full sample	5.511	0.748	0.008	0.756	0.750	0.008	0.757	4.474	0.250	4.586	0.254	0.00025	-0.00079

Table 2. The number density (n), different components of the shear response ($R_{\gamma/S/\text{tot},1/2}$), effective number density of source galaxies (n_{eff}) and shape noise (σ_e) in the H12 and C13 definitions, and the mean weighted shear ($\langle \gamma_{1,2} \rangle$), all computed for each of the tomographic bins as well as the full non-tomographic sample. The number densities are calculated with an area of $5,412 \text{ deg}^2$, and are presented in units of $1/\text{arcmin}^2$.

statistical precision to the DES Y3 shape catalog. Table 2 also includes the weighted, calibrated mean shear in each bin. The mean γ_2 in some bins (particularly bin 3 and 4) is relatively high in our data. This mean shear is subtracted following GS21 and Yamamoto & Becker et al. (2025). In the tomographic analyses performed in the other works of this series (PAPER II; PAPER III; PAPER IV), we subtract a mean shear per tomographic bin. We note that a non-zero mean shear

has also been found in the aforementioned DES works but its origin is unclear. In PAPER III (see their Section 6) we analyze forty-six different half-splits of the shape catalog, and find they return statistically consistent cosmology constraints. The tomographic bin-dependent mean shear can vary under each split (since a split alters the selection of the shape catalog), with the 95% range across splits roughly spanning $\delta \langle \gamma \rangle \approx 5 \times 10^{-4}$ for the two shear components and the different tomographic

bins.

4 EMPIRICAL SHEAR TESTS

Following the convention in the community (Jarvis et al. 2016; Zuntz & Sheldon et al. 2018; Gatti & Sheldon et al. 2021; Giblin et al. 2021; Li et al. 2022; Yamamoto & Becker et al. 2025), we perform a number of tests to ensure our shape catalog is not impacted by systematic biases associated with instrumental or observational effects. These are primarily null tests that verify the quality of (or reveal oddities in) our data through analyses that use only the data itself (*i.e.*, without any simulations). Such tests do not isolate the exact origin of any detected oddities, but finding a statistically significant signal in any null test is a sign of concern and necessitates further investigation into the data. These tests are especially important in our case, as we are working with a somewhat unconventional weak lensing dataset where new effects could be relevant.

One of the primary systematic sources that can generate spurious shear is the imperfect modeling of the PSF. This is of particular concern because the PSF can contain spatial correlations which would then mimic the cosmological signal. Furthermore, we use a different algorithm (PSFEx) for the PSF modeling compared to that used in the most recent DES analyses (PIFF, Jarvis et al. 2020), so these tests check that the quality of our PSF model is still sufficient for cosmological inference of this data. Tests associated directly with the PSFs are described in Sections 4.1, 4.2, 4.3, part of 4.4, and 4.5. The PSF star sample used for these tests is detailed in Appendix A3.

In Section 4.6, we describe other tests that could be indirectly related to the PSF modeling systematics as well as other spatially varying systematic effects in the instrument and data. In Section 4.7 we also test potential contamination in the shear measurements associated with observing conditions of the imaging data, and in Section 4.8 we quantify the B -mode contribution to our shape catalog.

For tests involving the spatial correlation of PSF ellipticities — the Rowe/Tau stats (Section 4.5) and tangential shear (Section 4.6) — we follow GS21 in using a star weight for each PSF star. GS21 found that PSF stars are preferentially detected in regions with fewer galaxies due to the star-finding algorithm failing in crowded regions of the sky. Thus the number counts of the detected PSF stars is anti-correlated with the large-scale structure. This is unideal for the tangential shear test as we will then find a slight, negative correlation in the tangential shear around stars. Following GS21, we correct for this effect by weighting all PSF stars with $w = n_{\text{gal}}/n_{\text{star}}$. We make a HEALPIX map of the galaxy number density, n_{gal} , and of the star number density, n_{star} , with a resolution of $\text{NSIDE} = 512$ (we have verified the robustness of our results to

different choices of NSIDE). The weight map is then generated as the ratio of the two maps and stars are assigned the weight of the pixel corresponding to their position on the sky. These weights also have the secondary effect of optimizing our null test statistics by preferentially upweighting measurements at the locations of galaxies.

4.1 Mean PSF in focal plane

Figure 5 shows a visual example of the PSF modelling errors in the data. In particular, it shows the residuals in the PSF model across the full focal plane of DECam, averaged over all riz -band exposures used in this work. We see consistent patterns when compared to DES Y3 (see e.g., Figure 9 in Jarvis et al. 2020), *i.e.*, large-scale fluctuations in $e_{1,2}$ due to the polynomial order used in the PSF model interpolation, and CCD-scale fluctuations in the PSF size T_{psf} (“tree rings”) due to impurities in the CCD silicon (Estrada et al. 2010; Plazas et al. 2014a,b). The similarity between DES and DECADE in the structure of these residuals is expected since the dominant contribution to these residuals are the optics and instrument systematics, which are the same across both datasets. Differences due to atmospheric conditions, which *can* vary between DES and our dataset, are suppressed as we average over many exposures. Figure 5 also shows that there are 1.5 additional CCD chips being used in our work compared to DES Y3 (the middle chip in the top row, CCD2, and the upper channel in the right-most chip in the 6th row, CCD31). DES Y3 took a conservative approach and discarded these data for shear measurements as the CCD chip/channel was not functioning for a subset of the survey period. In this work, we include these data as they have no problems apart from the fact that we discard data from these CCDs during the time period in which they malfunctioned. Note that these data have gone through extensive quality control and visual inspection (see Section 2.1).

4.2 Brighter-fatter effect

The brighter-fatter effect (BF, Antilogus et al. 2014; Guyonnet et al. 2015; Gruen et al. 2015) refers to a nonlinear sensor effect in the CCD, where the charge carriers induced by incoming photons are deflected by the accumulated charge at bright spots. A consequence of this effect is that brighter stars appear to be larger in the CCD images, which presents a challenge to PSF modeling as the models are built using the light profile around stars. To circumvent this effect, as well as other effects associated with bright stars (such as saturation), we do not use very bright stars for PSF modeling (see Appendix A). Furthermore, the CCD images are corrected to account for the BF effect (Gruen et al. 2015). Therefore, in this test we examine any remaining BF effect (after image corrections) in the stars that are used for PSF modeling.

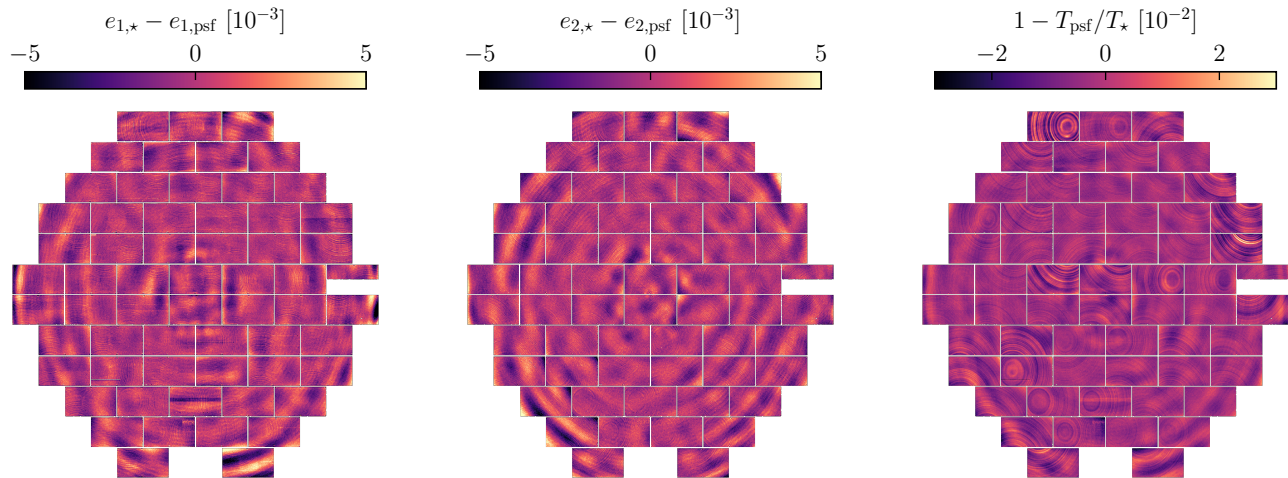


Figure 5. The mean PSF ellipticity error (left, middle) and size error (right) across the DECam focal plane. The large-scale, correlated modes in the ellipticity errors are from interpolation errors in the PSF model and follows those observed in DES (Jarvis et al. 2020). The size errors show small-scale features that are localized to individual CCDs, and these are “tree rings” arising from impurities in the silicon used in the sensors (Estrada et al. 2010; Plazas et al. 2014a,b).

The BF effect is estimated by evaluating our PSF models at the location of the PSF stars and comparing the size and shape of the measured star to that inferred from the PSF model. The measurements of the star shape and size are performed via the GALSIM package (Rowe et al. 2015), using implementations of the HSM algorithms as developed in Hirata & Seljak (2003); Mandelbaum et al. (2005). This comparison of the PSF model and the star measurement is done as a function of the star’s magnitude in the relevant band. In Figure 6, we show the error and fractional error in the PSF model size (top and middle) and the error in the PSF ellipticity (bottom) as a function of the star brightness. The results combine measurements from the *riz* bands, and the error bars — which in almost all cases are much smaller than the points — are derived via jackknife resampling from 150 spatial patches. The patch locations and assignments are constructed by passing the sky locations from the object catalog into the optimized k-means clustering algorithm in TREECORR (Jarvis et al. 2004).

We observe a clear trend where the PSF size inferred from the model tends to be bigger (smaller) than the measured values from the fainter (brighter) stars. This is expected as the PSF model is constructed using stars of all magnitudes (*i.e.*, it is averaged across all magnitudes), and the BF effect will cause bright stars to appear larger, thus generating positive residuals towards the bright end in our plots. The fractional error in PSF sizes due to this effect is at the $10^{-3} - 10^{-2}$ level, which would propagate as an additive bias to shear at the $10^{-5} - 10^{-4}$ level (assuming the PSF ellipticity is at the level 10^{-2}); see Equation (15). The error in the e_1 and e_2 of the PSF model also shows a magnitude-dependent trend. These appear at the 10^{-4} level, with e_2 monotonically decreasing with magnitude and e_1 having a more complicated shape. The amplitude in

both cases is consistent to that found in DES Y3 (GS21, see their Figure 6).

For both this test, and those to follow (particularly in Section 4.3 and 4.4), we treat additive terms of $\delta e \lesssim 2 \times 10^{-4}$ as negligible. This is motivated in three quantitative ways: (i) first, we expect a non-zero mean shear in our catalog due to cosmic variance. We estimate this for our data using jackknife resampling of the catalog, and find $\sigma(\langle \gamma \rangle) \sim 0.6 \times 10^{-4}$. This is broadly consistent with the value quoted in DES Y3, $\sigma(\langle \gamma \rangle) \sim 0.5 \times 10^{-4}$, which was estimated using simulated mock catalogs. Thus, additive terms with amplitudes at/below $\sim 2 \times 10^{-4}$ are within the 3σ limit defined by cosmic variance. (ii) The mean shear of our catalog is of the order $\sim 5 \times 10^{-4}$ (this value is the average of $|\langle e_1 \rangle|$ and $|\langle e_2 \rangle|$, see Table 2). Following GS21, the mean shear per-component is subtracted from the catalog before performing cosmic shear measurements. Thus, additive terms with amplitudes below this mean shear can be treated as negligible. Finally, (iii) the additive bias, c (see Equation 20) estimated in the image simulations is of the same order, $\sim 5 \times 10^{-4}$ (Table 4). Under these considerations, the trend of the mean PSF ellipticity with magnitude is negligible. Note that in Section 4.5 we explicitly show the impact of these PSF model errors on the measurements relevant for cosmological inference, and find that the impact is negligible. Figure A1 in PAPER III also shows that the impact of such model errors on our final cosmology constraints is negligible.

4.3 PSF color dependence

Next, we check the color-dependence of our PSF model. It is well-understood that the PSF is wavelength-dependent –

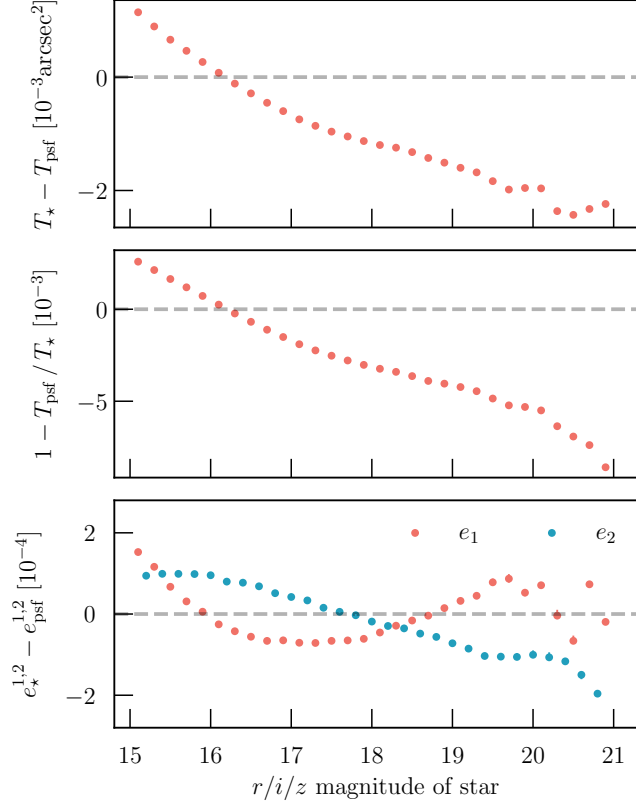


Figure 6. The brighter-fatter effect as found in the size residual (top panel), fractional size residual (middle panel), and shape residual (bottom panel), where the residuals are the difference between the star and the PSF model evaluated at the location of the star.

photons of different wavelength traverse differently through the atmosphere, optics, and detector, resulting in a different PSF at that specific wavelength. The PSF model is constructed using observations of stars, which generally have a more blue-tilted spectral energy distribution (SED) relative to galaxy SEDs. When applying this model for PSF-deconvolved shape measurements of galaxies, we are using a slightly incorrect model given the galaxy SED is different from the stars’. The effect is more severe when the filter band covers a broader wavelength range. A detailed investigation for the DES Y3 data can be found in [Jarvis et al. \(2020\)](#), and an improved color-dependent PSF model is used in DES Y6 ([Schutt et al. 2025](#)). Our image data was already processed using a color-independent PSF model, but we quantify any residual PSF contamination in our shear estimates (*e.g.*, due to imperfect PSF modelling) using the Rowe/Tau statistics; see Section 4.5. This is similar to the approach used in DES Y3, which also had a color-independent PSF model.

The most relevant contributor to the color-dependence is the effect of differential chromatic refraction (DCR, [Plazas & Bernstein 2012](#); [Meyers & Burchat 2015](#)), where the PSF is preferentially elongated along the direction towards zenith

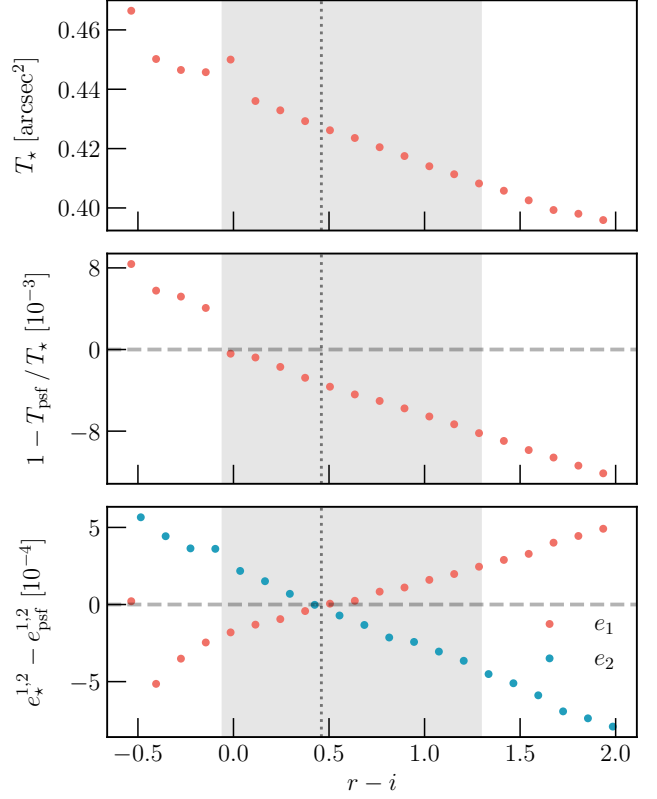


Figure 7. The variation in the PSF as a function of color, in this case $r - i$. The gray vertical band (dotted line) shows the 95% region (median) of the $r - i$ color for the galaxy sample. The size varies by 0.02 arcsec^2 over most of the color range. The fractional error changes by 1%, and the shear error changes by around 2.5×10^{-4} .

with the elongation being stronger for sources with bluer colors compared to those with redder colors. This effect is particularly important when using the DECADE shape catalog for cosmic shear as (i) the image data extends to higher airmass than DES and (ii) this effect could potentially imprint a spatially correlated bias instead of a stochastic, random bias.

Figure 7 shows the size of the PSF model and errors in the model size and ellipticity, all as a function of the $r - i$ color of the star. The gray band shows the 95% region of colors spanned by the source galaxy sample. The PSF size error varies by $< 1\%$ across this range, while the mean PSF ellipticity error has an amplitude below 2.5×10^{-4} across this same range. Following the same argument in Section 4.2, this residual error will not impact our cosmology analysis. In Section 4.5 we quantify the impact of the additive PSF systematics on the data vectors relevant for cosmology. In [PAPER III](#), we also derive cosmology constraints using only the high/low airmass region of our survey and find the constraints are consistent with each other.

We note that the results of Figure 7 require a matching procedure. Since a PSF star is an exposure-level object, it

only contains information about a single band. Thus, we have to assign a color to each star via a matching procedure on the sky. Briefly, we match stars across bands and exposures to assemble a “catalog-level coadd” and derive a color estimate averaged across exposures. We then assign that color estimate to each exposure-level star measurement. The catalog-level coadd is done by taking all stars in the (exposure-level) PSF star catalog and grouping together those stars with sky positions within a given HEALPIX pixel. We choose NSIDE = 262144 as it corresponds to a pixel scale of $0.8''$, close to the $0.5''$ matching radius used in other techniques within DES and our work. Each pixel — which can now be treated as a separate star given the resolution of the map — is then assigned a magnitude in each band by taking the weighted average of all available magnitude estimates of a given band, in that pixel. The weights used in the averaging are the signal-to-noise of each exposure-level measurement of the star. After assigning each pixel a set of *riz* magnitudes (and the colors derived from the magnitudes), each star in the original, exposure-level catalog is assigned the colors of the pixel associated with its position on the sky.

4.4 Mean shear as a function of METACALIBRATION quantities

Next, we examine the correlation between our shear estimate with other quantities measured in METACALIBRATION, such as PSF size (T_{psf}), PSF ellipticity ($e_{\text{psf}}^{1,2}$), galaxy color, galaxy signal-to-noise (SNR), and ratio of galaxy size to PSF size (T/T_{psf}). We divide the galaxies into 20 equal-count (*i.e.*, percentile) bins, where the binning is done on the quantity we are correlating the shear estimate with. The mean shear in each bin is computed while using the shear weights and then calibrated using the response computed bin-by-bin. The response used here is the total response given in Equation (3) and also includes the selection term corresponding to the binning procedure. The correlation between shear and a given quantity is estimated via a linear regression. We fit the model

$$\langle \gamma^{1,2} \rangle = \alpha^{1,2} X + \beta^{1,2}, \quad (13)$$

where X is the quantity of interest and α , β are the free parameters. A significant detection of α indicates that the mean shear is dependent on X . Figure 8 presents the results of this test. The data points show the measured, mean shear per bin while the dashed line shows the fit from the regression. The slope of the linear fit and its associated significance are shown in the legend. The uncertainty used to quantify the significance is obtained via jackknife resampling with 150 spatial patches.

With few exceptions, the significance of the slope is consistent with zero within 3σ . The most significant correlation is of shear with galaxy color, which is expected

given the impact of DCR on the PSF modelling error and thereby the impact on the galaxy shapes. We note that the contribution of PSF correlations to the shear correlation functions is quantified, and found to be negligible, in Section 4.5 below. Figure 8 shows that the variation of the mean shear across bins for different quantities is generally within $\Delta e = 2 \times 10^{-4}$, which is negligible for the same arguments discussed in Section 4.2. We note that there is a slight increase of the mean shear, $\langle \gamma_2 \rangle$, for objects at low SNR and this increase is similar to the result in DES Y3 (GS21, see their Figure 21), who confirmed that such an effect is completely negligible on cosmological constraints.

4.5 Rowe statistics and Tau statistics

A key empirical test in all shear-related analyses is quantifying the impact of PSF systematic effects on the measured data vectors. PSF shapes can be correlated across the sky either due to the true PSF’s intrinsic ellipticities (for example, from effects like DCR) or due to modeling/interpolation errors in the PSF model. The latter occurs because the PSF is modelled using test points (*i.e.*, stars) at a sparse set of locations on the focal plane and this model is then interpolated to the locations of galaxies. Thus, any errors in the interpolation will be shared by neighboring galaxies on the focal plane. The PSF modeling error is typically assumed to be additive, *i.e.*, our estimated shear γ differs from the true shear γ^{true} by an additive factor that depends on the PSF model $\delta e_{\text{psf}}^{\text{sys}}$ and noise. That is,

$$\gamma = \gamma^{\text{true}} + \delta e_{\text{psf}}^{\text{sys}} + \delta e^{\text{noise}}. \quad (14)$$

Motivated by Paulin-Henriksson et al. (2008) and Jarvis et al. (2016), we parametrize $\delta e_{\text{psf}}^{\text{sys}}$ via

$$\begin{aligned} \delta e_{\text{psf}}^{\text{sys}} &= \alpha e^{\text{psf}} + \beta (e^{\star} - e^{\text{psf}}) + \eta \left(e^{\star} \frac{T^{\star} - T^{\text{psf}}}{T^{\star}} \right), \\ &\equiv \alpha \mathbf{p} + \beta \mathbf{q} + \eta \mathbf{w}. \end{aligned} \quad (15)$$

That is, we identify three quantities that capture both the PSF model and its error, up to the second moment: $\mathbf{q} \equiv e^{\text{psf}}$ is the ellipticity of the PSF model; $\mathbf{q} \equiv e^{\star} - e^{\text{psf}}$ is the error in the ellipticity estimated as the difference between the ellipticity of the true PSF as measured from stars and of the PSF model evaluated at the location of the stars; and $\mathbf{w} \equiv e^{\star} (T^{\star} - T^{\text{psf}}) / T^{\star}$ is the true PSF ellipticity multiplied by the fractional error in the size of the PSF model. Given these three quantities, we can write a set of six terms describing the two-point correlations between them (Rowe 2010; Jarvis et al.

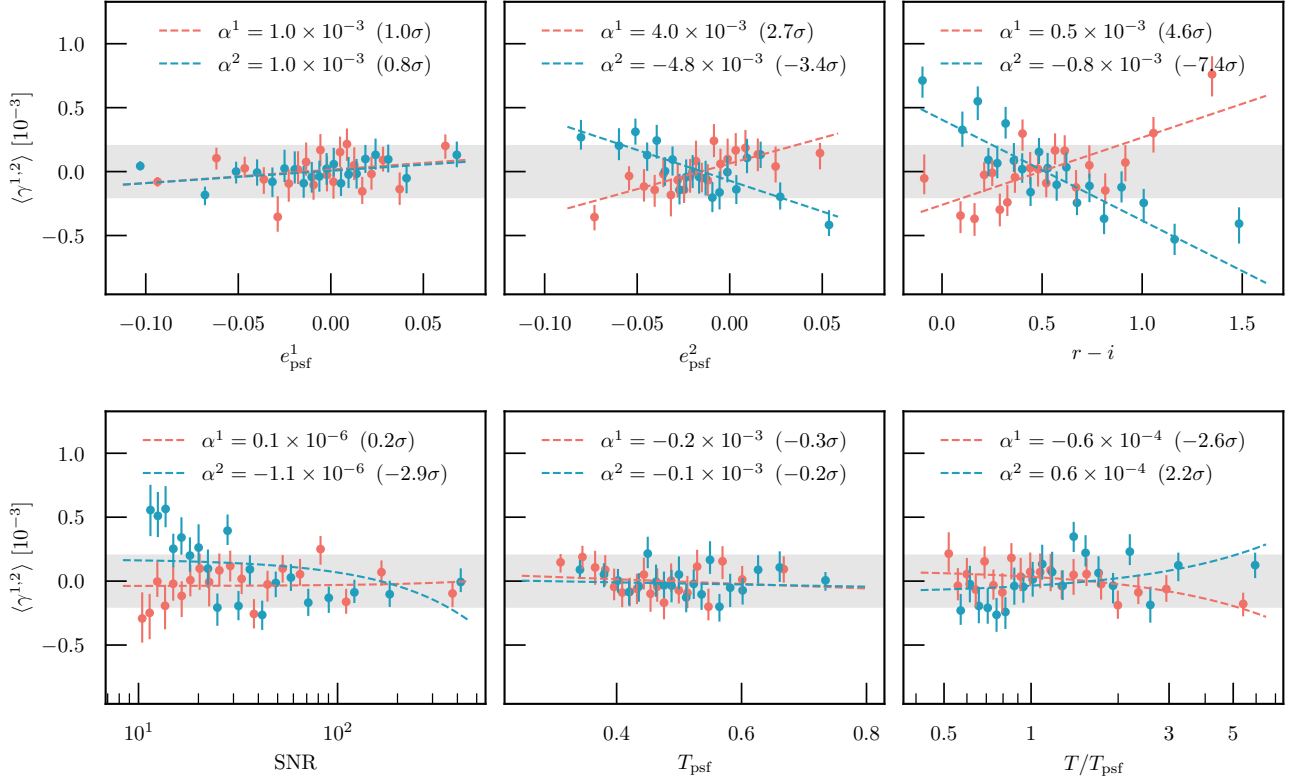


Figure 8. The mean shear of our fiducial sample, in percentile bins defined using other METACALIBRATION quantities. The mean shear is calibrated by a response that is computed bin-by-bin. Note that the PSF ellipticity and sizes used above are now measured within METACALIBRATION. The dots show the measurements while the dotted line is a linear regression. The legends quote the slope and the significance α/σ_α , where the uncertainty is estimated through 150 jackknife resamplings. The gray band shows the $\Delta e = 2 \times 10^{-4}$ region, and almost all points fall within this range.

2016):

$$\begin{aligned}
 \rho_0 &= \langle \mathbf{e}^{\text{psf}} \mathbf{e}^{\text{psf}} \rangle = \langle \mathbf{p} \mathbf{p} \rangle, \\
 \rho_1 &= \langle (\mathbf{e}^\star - \mathbf{e}^{\text{psf}})(\mathbf{e}^\star - \mathbf{e}^{\text{psf}}) \rangle = \langle \mathbf{q} \mathbf{q} \rangle, \\
 \rho_2 &= \langle \mathbf{e}^{\text{psf}}(\mathbf{e}^\star - \mathbf{e}^{\text{psf}}) \rangle = \langle \mathbf{p} \mathbf{q} \rangle, \\
 \rho_3 &= \langle (\mathbf{e}^\star(T^\star - T^{\text{psf}})/T^\star)(\mathbf{e}^\star(T^\star - T^{\text{psf}})/T^\star) \rangle = \langle \mathbf{w} \mathbf{w} \rangle, \\
 \rho_4 &= \langle (\mathbf{e}^\star - \mathbf{e}^{\text{psf}})\mathbf{e}^\star(T^\star - T^{\text{psf}})/T^\star \rangle = \langle \mathbf{q} \mathbf{w} \rangle, \\
 \rho_5 &= \langle \mathbf{e}^{\text{psf}}\mathbf{e}^\star(T^\star - T^{\text{psf}})/T^\star \rangle = \langle \mathbf{p} \mathbf{w} \rangle.
 \end{aligned}
 \tag{16}$$

These are commonly known as *Rowe statistics* (Rowe 2010) and have been used in other works as diagnostics for the PSF modeling error (Jarvis et al. 2016; Gatti & Sheldon et al. 2021; Yamamoto & Becker et al. 2025; Schutt et al. 2025). We note that recent analyses, motivated by the findings of Zhang et al. (2023), have included additional terms in the Rowe Statistics that capture higher-order contributions (Dalal et al. 2023; Li & Mandelbaum 2023; Yamamoto & Becker et al. 2025; Schutt et al. 2025). In this work, we follow the DES Y3 choices and do not include such higher-order terms. We note that Zhang et al. (2023, see their Figure 16) also show the impact of PSF contamination on cosmology is negligible

regardless of whether these additional, higher-order PSF terms are included/excluded in the analysis.

The Rowe statistics measure the spatial correlations of the PSF model and of the modelling errors, summarized here via two-point statistics on the sky. These statistics, however, do not quantify the level of contamination this non-cosmological correlation introduces into the cosmic shear measurement, *i.e.*, it does not quantify the values of the coefficients α , β , τ in Equation (15). A second set of statistics, the *Tau statistics*, is used to estimate these coefficients and thereby show the impact of PSF-related spatial correlations on the shear correlations. The Tau statistics are measured by correlating the three PSF-related quantities above with our galaxy shape catalog:

$$\begin{aligned}
 \tau_0 &= \langle \boldsymbol{\gamma} \mathbf{p} \rangle = \alpha \rho_0 + \beta \rho_2 + \eta \rho_5, \\
 \tau_2 &= \langle \boldsymbol{\gamma} \mathbf{q} \rangle = \alpha \rho_2 + \beta \rho_1 + \eta \rho_4, \\
 \tau_5 &= \langle \boldsymbol{\gamma} \mathbf{w} \rangle = \alpha \rho_5 + \beta \rho_4 + \eta \rho_3.
 \end{aligned}
 \tag{17}$$

The system of equations above can be solved to estimate α , β and η , and thereby the contamination of PSF-related spatial correlations in our shear correlation function.

The Rowe statistics of our catalog are estimated using

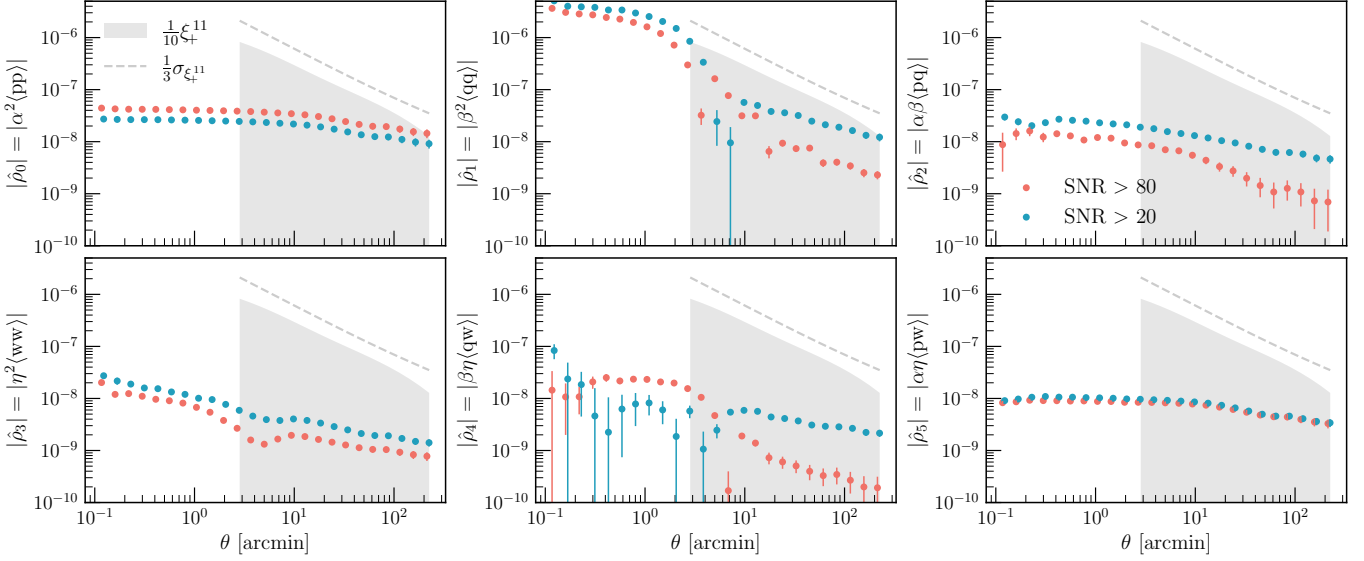


Figure 9. The ξ_+ component of the spin-2 correlation function defined by the PSF quantities: the ellipticity p , the ellipticity error q , and the size error w . We multiply the correlations by the coefficients α, β, η which quantify how the former propagate into the measured shear. See text for details on these coefficients. Here, we have used the 68% upper bound (on the absolute value) for the coefficients rather than the best fit value as the former is a more conservative estimate. The gray band (dashed line) shows 10% of the smallest cosmological signal (one-third of the smallest measurement uncertainty) in our data vector, from the autocorrelation of the 1st tomographic bin. In all cases the PSF signal is subdominant. This is true even if we vary the SNR threshold of the star sample used to estimate the Rowe statistics. This test serves an order-of-magnitude estimate of PSF contamination, and a test showing the negligible impact of this contamination on cosmology constraints is presented in [PAPER III](#).

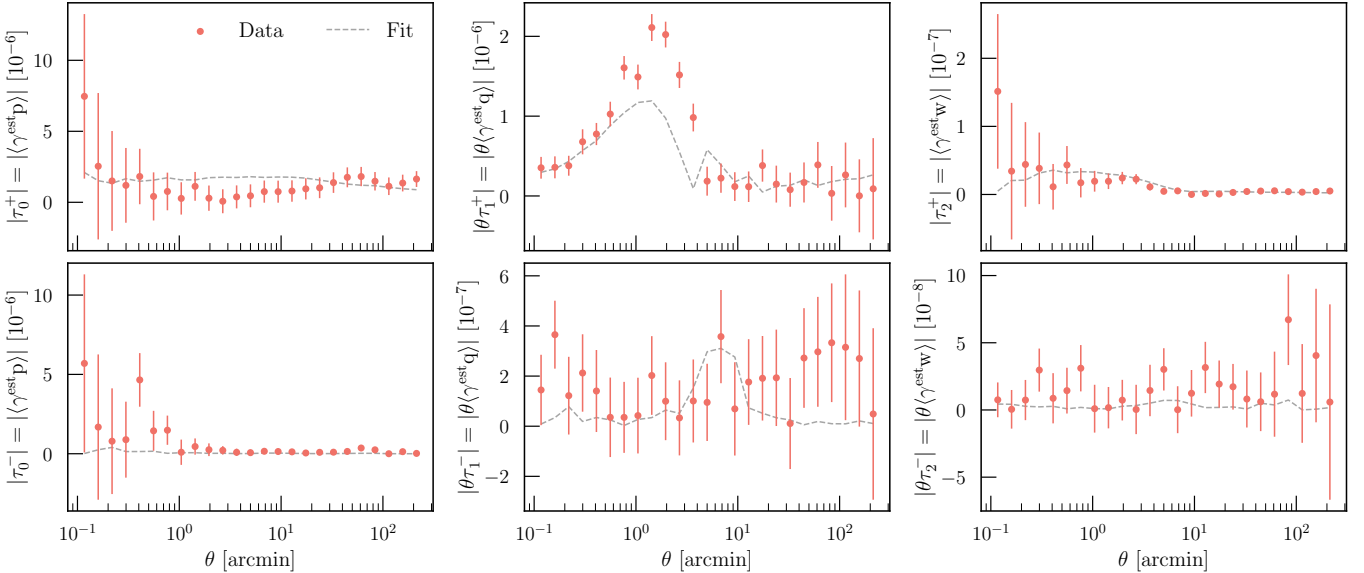


Figure 10. The Tau statistics of the shape catalog, which quantify the correlation between the estimated shear and the PSF terms. The red points show the measurement and the associated uncertainties, while the gray dashed lines are the fits to the measurement using the Rowe stats as templates; see Equation (17). The fit is characterized by a p-value of $p = 0.46$. Note that the data points all have strong correlations with one another, as is also noted in [GS21](#).

TREECORR (Jarvis et al. 2004) and are presented in Figure 9. The error bars are generated via jackknife resampling of 150 patches.¹¹ All quantities (\mathbf{p} , \mathbf{q} , \mathbf{w} and $\boldsymbol{\gamma}$) are mean-subtracted before calculating the correlation and $\boldsymbol{\gamma}$ is also calibrated using the response, $\langle \mathbf{R} \rangle$. The presented measurements in Figure 9 are scaled by the relevant factors of α , β and η , and thus the lines represent the level of contamination introduced by the PSF-related spatial correlations. The overlaid gray bands show 10% of the expected cosmic shear signal in the lowest redshift bin (*i.e.*, the bin where the amplitude is the lowest), using the redshift distribution found in PAPER II. The gray dashed line also shows 1/3rd of the expected uncertainty (0.3σ) on the shear measurement, estimated using the covariance model of PAPER III. Both references are plotted only for the scales where we perform cosmic shear measurements ($2.5' < \theta < 250'$), but the Rowe statistics measurements extend to smaller scales. We observe that all the Rowe statistics are within the grey band, indicating the PSF model errors are subdominant to the cosmological signal. An explicit test of the impact of PSF contamination on cosmology constraints is shown in PAPER III. We also tested for several SNR cuts in the star samples (see also Appendix A) and find that the results from the Rowe statistics are relatively stable (*i.e.*, the correlations' amplitudes vary by less than a factor of 2) once we cut above $\text{SNR} > 40$. Note that we use the star weights described above to weight the PSF stars, but our findings of negligible PSF contamination do not change if we ignore these weights.

In Figure 10 we present the full set of Tau statistics together with the best-fit of the model described in Equation 17. The fit is done using a Monte Carlo Markov chain (MCMC) sampling routine from the EMCEE package (Foreman-Mackey et al. 2013). The best-fit values are $\alpha = 0.0023 \pm 0.0031$, $\beta = 1.081 \pm 0.074$ and $\eta = -0.394 \pm 0.926$, with the p -value of the fit given as $p = 0.46$. For a DES-like sample, we expect $\alpha \sim 0$, $\beta \sim 1$ and $\eta \sim 1$; for example, see Table 2 in GS21. Our estimates are consistent with these expectations.

4.6 Tangential shear around stars and field centers

Next we measure the mean tangential shear around PSF stars and field centers (*i.e.*, the center of an exposure in celestial coordinates). We expect both quantities to be zero in the absence of statistically significant, imaging-related

¹¹ We have checked that the results of the fits discussed below are similar even if we use 300 or 450 jackknife patches when estimating the covariance. The resulting values of α , β , η shift within their uncertainties, and we always find $p > 0.1$ for the best-fit. We account for the Hartlap factor (Hartlap et al. 2007) in all cases. This indicates that any errors in our jackknife-based covariance estimate do not significantly affect the results of the test. We also note that recently, Guerrini et al. (2024) introduced a semi-analytic method of covariance estimation that circumvents the limitations of the jackknife-based one. We have not used this technique as it was published after our catalog tests were already concluded, and also after our final cosmology results, in PAPER IV, were unblinded.

systematics in the shape catalog.

The tangential shear for a single source galaxy i with respect to some reference location j is defined as

$$\gamma_t^{ij} = -\gamma_1^i \cos(2\phi^{ij}) - \gamma_2^i \sin(2\phi^{ij}), \quad (18)$$

where ϕ^{ij} is the angle between the line connecting the source i and reference point j , and the declination-axis of the sky coordinate system (Bartelmann & Schneider 2001). In our case, the reference points are either field centers or stars. For the full shape catalog, we calculate

$$\gamma_t(\theta) = \frac{\sum_{ij} w_{SX}^{ij} \gamma_{t,SX}^{ij}(\theta)}{\sum_{ij} w_{SX}^{ij}(\theta)} - \frac{\sum_{ik} w_{SR}^{ik} \gamma_{t,SR}^{ik}(\theta)}{\sum_{ik} w_{SR}^{ik}(\theta)}, \quad (19)$$

where the first term sums over all sources i and reference points j (SX refers to source-reference point), and the second term sums over all sources i and randoms k (SR refers to source-random). The source-galaxy shears are weighted by the METACALIBRATION weights w_S^i (Equation 8), are mean-subtracted, and are calibrated with the response. The reference points are weighted by w_X^j , and the specific choice of weights is described further below. The random points we generate are distributed uniformly in the shape catalog footprint and are weighted by w_R^j , which is proportional to the number of galaxies in that location of the sky. The combined weights are $w_{SX}^{ij} = w_S^i w_X^j$ and $w_{SR}^{ik} = w_S^i w_R^k$.

In Figure 11 we show the tangential shear measurement for stars (upper panel) and the field centers (lower panel). All measurements are performed with TREECORR (Jarvis et al. 2004) and the error bars are estimated via jackknife resampling of 150 jackknife patches. Note that the datapoints on large-scales ($\theta > 20'$) are all highly correlated.

For the PSF stars, we further split the star sample into a bright and a faint sample based on their magnitudes in the band corresponding to a given exposure. Following DES Y3 (GS21), we split on $m_X \leq 16.5$ in band X. A non-zero tangential shear signal can be generated around bright stars due to significant artifacts (background subtraction, masking) near such stars that subsequently impacts the shear measurements of nearby galaxies. A tangential shear signal can also be generated around faint stars due to the standard PSF modelling errors we have discussed above. While the Rowe stats in Section 4.5 have already validated our catalog, this test provides further validation as is it a different type of shear measurement. For both subsamples, we find no statistically significant tangential shear measurement. The p -values of the data vector are $p = 0.52$ and $p = 0.11$ for the bright and faint sample, respectively.

In this test the PSF stars are weighted by $w_X = n_{\text{gal}}/n_{\text{star}}$ as discussed earlier. The random sample is weighted by $w_R = n_{\text{gal}}$. The PSF star weights can be viewed as performing two

distinct functions: (i) they transform a star sample that is spatially inhomogeneous into one that is uniformly distributed, and (ii) they upweight the sample in locations of galaxies so that the subsequent measurements are upweighted in those locations. The random sample we generate is already uniform and therefore does not need step (i). Thus, we perform only step (ii) for the randoms.

As for the shear around field centers, a non-zero signal can indicate correlations of the measured shear with focal plane coordinates. For example, in Figure 5 we have shown the correlation of PSF modelling errors with focal plane coordinates. However, there can exist other correlations as well. The field center catalog is the central R.A. and Dec. of the 42,700 exposures that correspond to the shape catalog described in Section 3. Note that we remove all field centers that do not pass our foreground mask. The tangential shear measurement around field centers is consistent with zero with a p-value of $p = 0.24$.

Similar to the PSF star case, we generate weights for the field centers as $w_X = n_{\text{gal}}/n_{\text{fc}}$. Similar to n_{gal} and n_{star} , n_{fc} is estimated as the number of field centers in a HEALPIX pixel of NSIDE = 512. All field centers are assigned an n_{fc} value from the pixel corresponding to their location on the sky. This term, $1/n_{\text{fc}}$, is required in the weights as the locations of exposures used in our data are not uniform; given our use of data from community programs, which often target specific sources/regions, there are more exposures in regions with large-scale structure. Therefore the tangential shear signal around field centers will be contaminated by the actual cosmological signal. We correct for this using these field center weights. The randoms once again are weighted by $w_R = n_{\text{gal}}$.

4.7 Impact of observing conditions of the survey

We then test for any significant correlations between the estimated galaxy shear and various quantities related to the observing conditions of the DECADE image data. Such a correlation could be non-zero if, for example, the PSF modeling error — which is correlated with the estimated shear; see Equation (15) — is correlated with an observing condition, such as the seeing or airmass. The PSF contamination effects, however, have been tested extensively in the sections above. Our test below probes the correlation between the shear measurements and a number of general observing conditions in our survey.

We consider a range of quantities: airmass, DCR, magnitude limit (or depth), exposure time, seeing, sky variation, sky background, and exposure number counts, with each quantity also split across the individual *riz* bands. All maps have a native resolution of NSIDE = 4096 and

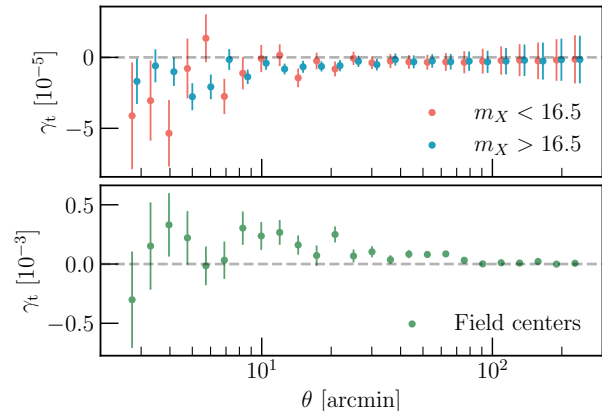


Figure 11. The tangential shear around PSF stars (top) and field centers (bottom). For the former, we measure the shear around both bright (red) and faint (blue) stars, split at $m_X \leq 16.5$ in the relevant band. Field centers are the center (in celestial coordinates) of all exposures used in generating the shape catalog. The tangential shear around both stars and field centers is consistent with no signal, at p-values of 0.52, 0.11, and 0.24 for the bright star, faint star, and field center catalogs, respectively. Note that the datapoints are highly correlated, particularly on large-scales ($\theta \gtrsim 20'$)

are generated from the individual CCD properties using the DECASU codebase¹² as is done for DES Y6 (Bechtol et al. 2025). Figure 12 shows an example of some of these survey property maps.

To test the correlation of these maps with shear, we first make weighted-average maps of the response-calibrated γ_1 and γ_2 from the shape catalog. The response is computed pixel-by-pixel. To reduce the impact of noise in the response estimate, we take the average response in HEALPIX pixels of NSIDE = 128 (corresponding to $\approx 30'$). At this resolution, a single pixel contains roughly 4 CCD images. Our results below are qualitatively similar if we use NSIDE = 256. Given the maps of the survey properties and the mean shear, we fit a linear model between the pixel values of the two and extract the slope. We quantify the uncertainty on the slope using 150 jackknife patches. Figure 13 shows the results for the detection significance of the slope, in all three bands. All slopes are consistent with zero within 2σ . The largest significance is for the correlations with the DCR maps and for the bluest band (*i.e.*, the *r*-band correlation is larger than *i*-band and *z*-band). Note that the first 5 maps presented — airmass, dcr_e1, dcr_e2, dcr_ddec, dcr_dra — are all highly correlated as they derive from either the zenith angle or from both the zenith and the parallactic angles (see Equations 7.6 and 7.7 of Jarvis et al. 2020) of the observations. Overall, we find there are no statistically significant correlations of the mean shear with the survey observing conditions.

¹² <https://github.com/erykoff/decasu>

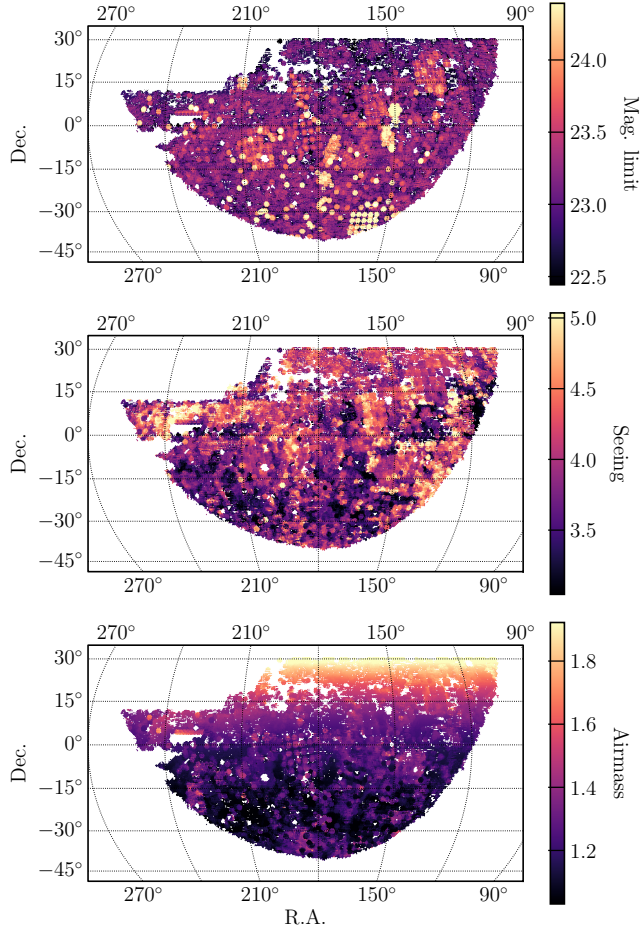


Figure 12. Example maps of the survey observing conditions. From top to bottom we show the magnitude limit (depth), the seeing (FWHM of PSF in pixel units), and airmass. All maps are shown in the i -band. Note that the source galaxy number density is significantly more homogeneous than the depth map (see Section 2.3 and also Figure 1 in PAPER III).

4.8 B -modes

Finally, we measure the B -modes signal of our catalog, which is a test of other imaging systematics in the data. Shear is a spin-2 field and can be mathematically decomposed into a curl-free and a divergence-free component, which we commonly refer to as E -modes and B -modes, respectively (Schneider et al. 2010). To first order, gravitational lensing does not generate any B -modes,¹³ and thus measuring a null signal in the B -modes is a powerful test of residual systematics in the shape catalogs.

There are many different estimators for B -modes that can be used to test for systematic effects in a shape catalog (Schneider et al. 2010; Becker & Rozo 2016;

¹³ At first order, the lensing field is the gradient of a scalar potential, and such a field has no curl mode by definition (Schneider et al. 2010).

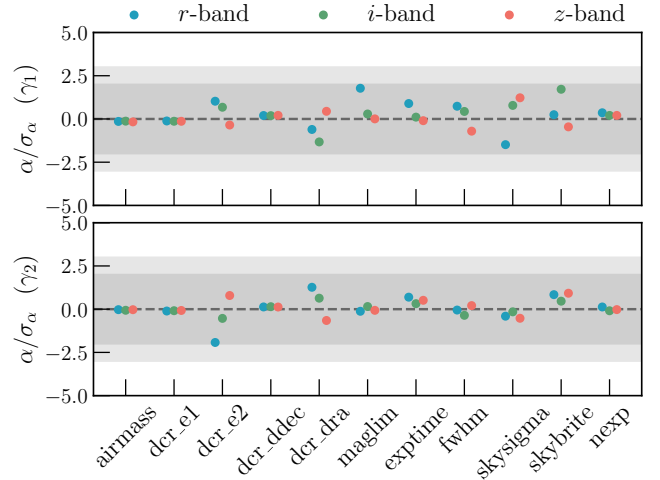


Figure 13. Significance of the slope (α) of a linear fit between the mean shear and survey observing conditions. From left to right the observing conditions are airmass, DCR in the e1 and e2 directions (with response to focal plane orientation), DCR in the R.A. and Dec. directions, the magnitude limit (or depth), the exposure time, the seeing (PSF FWHM), the standard deviation of the sky background, the sky brightness, and the number of exposures. The top (bottom) panel shows correlations with γ_1 (γ_2). All slopes are consistent with zero within 2σ (dark gray band). The lighter band is the 3σ region.

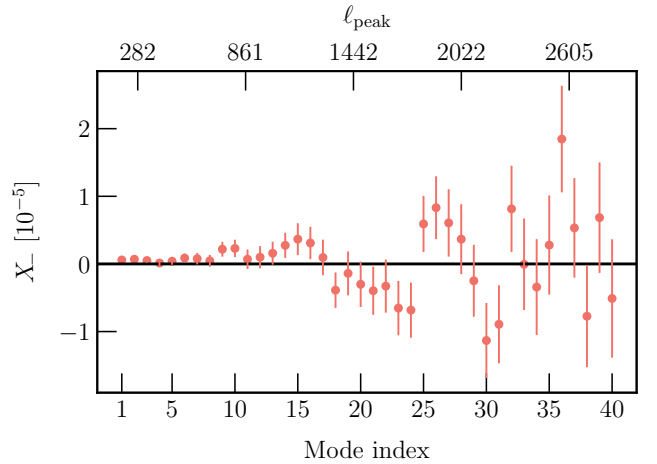


Figure 14. The B -mode amplitudes for 40 modes, estimated as a weighted sum of the $\xi_{+,-}$ correlation functions measured in 1000 bins between $2.5' < \theta < 250'$. The uncertainty estimates are obtained via 500 jackknife resamples. The measurements are consistent with null signal at $p = 0.11$, indicating this dataset has no statistically significant B -mode signal. The top axis shows the harmonic multipole corresponding to a given mode.

Alonso et al. 2019). We use the HYBRIDEB estimators developed in Becker & Rozo (2016), which derive B -mode amplitudes from measurements of the real-space correlation functions. This estimator has the advantage of determining the minimum/maximum angular scale in real-space, allowing us to measure B -modes for only scales corresponding to the data vector used in the cosmology analysis (here we use $2.5' < \theta < 250'$), and also allowing us to accurately incorporate the survey geometry without mixing E/B -modes. The B -mode amplitudes are computed as a weighted sum of the ξ_{\pm} correlations. We measure these correlations in 1000 logarithmic bins between $2.5' < \theta < 250'$ and then convert them into the B -modes amplitudes for 40 modes. The covariance matrix of ξ_{\pm} is estimated via jackknife resampling and then transformed into that of the B -modes. This transformation is trivial as the B -mode amplitudes are a linear combination of the correlation functions. In PAPER III we also estimate the B -modes for different tomographic bins of the shape catalog, using the harmonic-space estimator of Alonso et al. (2019), and find no evidence for B -modes.

The jackknife covariance matrix of ξ_{\pm} is now computed using 500 patches, rather than the fiducial choice of 150 patches. We found that using fewer realizations caused spurious, noisy correlations in the off-diagonal elements of the covariance that could then deteriorate the final χ^2 of the null test. Given our footprint is $5,412 \text{ deg}^2$, each of the 500 patches is still sufficiently large with an area of 11 deg^2 . We have also checked that the jackknife covariance matrix is qualitatively similar to those generated from simulation-based methods.¹⁴ We use the jackknife estimate of covariance for our null-tests, given this estimate is more reliable for capturing any/all effects in the dataset that contribute to the final covariance.

Figure 14 shows the B -mode amplitudes, denoted as X_{-} following the nomenclature of Becker & Rozo (2016). The measurement is consistent with the null signal at a p-value of $p = 0.11$. Therefore, we do not find B -modes in our catalog. We have also checked that the contribution of the PSF two-point correlation functions (Equation 16) to the B -modes is at least one to two orders of magnitude below the measurement above. As mentioned above, we also compute the B -modes per tomographic bin in PAPER III and find the measurement is consistent with no detection for all auto- or cross-correlation measurements.

¹⁴ For these methods, we make 150 mock catalogs by (i) randomly rotating all the galaxies in our catalog to get the shape noise, and then (ii) assigning each galaxy a cosmological shear based on its position, using lensing maps generated from the COSMOGRID simulations of Kacprzak et al. (2023) or the ULAGAM simulations of Anbajagane et al. (2024c); the former has a slightly higher resolution while the latter has a factor of $O(20)$ more independent sky realizations at fixed cosmology. The covariance is estimated by measuring B -modes for each of the mock catalogs.

5 SHEAR CALIBRATION BIAS

While in Section 4 we directly use the shape catalog to check for systematic biases, in this section we validate and calibrate our shear estimator. This is done by testing our shear measurement algorithms on image simulations, where the true shear of the sample is known. Similar to the approach in DES Y3 (MacCrann & Becker et al. 2022), these tests first validate the performance of the METACALIBRATION algorithm in ideal, simplistic simulations and then quantify the final uncertainties/biases on shear calibration using realistic image simulations.

The METACALIBRATION estimate described in Section 3.1 can be biased. Generically, this bias is written as,

$$\gamma_i^{\text{est}} = (1 + m)\gamma_i^{\text{true}} + c \quad (20)$$

where m is the multiplicative bias, and c is the additive bias (Heymans et al. 2006). In ideal conditions, the METACALIBRATION estimator is biased at $m \sim O(10^{-4})$, which a negligible effect (Sheldon & Huff 2017). However, under realistic conditions where sources are partially masked, blended etc., the multiplicative bias can be at the percent level. Estimates of additive bias in simulations are less vital as we subtract by the mean ellipticity of the catalog from each shape estimate, and thus the impact of the additive bias will be significantly reduced. Therefore, the calibration efforts in the community generally focus on the multiplicative bias, and we take the same approach here.

We use a suite of image simulations — that we specifically develop to mimic the processing framework of the DESDM pipeline used in the DECADE project — to calibrate these multiplicative biases. We describe the simulation pipeline in Section 5.1 and validate it in Section 5.2. Finally, in Section 5.3, we present the main result of our calibration: the final estimates for residual shear calibration bias, m , and their uncertainties, $\sigma(m)$. These will be an input to the final cosmology analysis (PAPER IV).

5.1 Image simulations pipeline

Our pipeline is developed following the approach of MacCrann & Becker et al. (2022). Briefly, the pipeline fully simulates CCD images by injecting synthetic galaxies and star models, adding noise, masks, background etc. associated with the image. Then, the entire DESDM pipeline is run on these CCD images to reproduce coadded images, SOURCEEXTRACTOR detection catalogs, METACALIBRATION shear estimates etc. We now describe each piece in more detail:

Coadd tile selection: We randomly select 1600 coadd tiles from across the footprint. A subset of the galaxies in

these tiles are in regions removed according to our foreground mask, and thus are not used in the calibration.

Galaxy sample: We use the same galaxy sample as MacCrann & Becker et al. (2022), which was obtained from one of the DES deep fields that overlapped with the COSMOS field (Scoville et al. 2007) and was imaged using the Hubble Space Telescope (HST). The availability of HST images with their significantly smaller PSF allows for the precise measurement of the galaxy shapes/morphology, while the availability of the DES images allows for measurements of DES photometry for these same galaxies. See Hartley & Choi et al. (2022) for more details on the DES-COSMOS deep fields catalog used as our input galaxy sample. MacCrann & Becker et al. (2022) perform additional quality cuts to obtain a purer sample of galaxies, and the same has been done for this work. In practice, we select all galaxies brighter than $i < 25.5$, which is two magnitudes deeper than the median survey depth of $i \approx 23.5$ (see Figure 1) and two magnitudes deeper than our i -band selection cut (see Section 3.2). The galaxy models are obtained from the FITVD method (Bechtol et al. 2025), which fits an exponential profile and deVaucouleurs profile to each galaxy image, representing the galactic disk and bulge, respectively. We use the NGMIX (Sheldon 2015) and GALSIM (Rowe et al. 2015) software packages to ingest the galaxy morphology and render an image of the galaxy.

Galaxy counts, shapes & positions: The number of galaxies in each tile is drawn from a Poisson distribution with a mean of $\langle N_{\text{gal}} \rangle = 160,000$. After processing the images through the DESDM pipeline and performing all cuts shown in Figure 1, we obtain a sample with $n_{\text{gal}} \approx 5$ gal/arcmin², similar to the raw number density of our data as shown in Table 2. First, all galaxy shapes are randomly rotated. Then, we apply a known, constant shear to all rotated galaxies. We chose $\gamma_1 = \pm 0.02$ and $\gamma_2 = 0$, following MacCrann & Becker et al. (2022), and the two variants (± 0.02) will be used for a noise suppression step discussed further below. The galaxy positions are placed randomly on the tile, and thus galaxies are allowed to be blended. Note that in the real sky the galaxy positions are correlated, which results in less blending of objects at similar redshifts. We follow MacCrann & Becker et al. (2022) in not incorporating this spatial correlation.

Simulated star catalog: To improve the realism of our synthetic images, we inject simulated stars. We use the star catalog of Dal Tio et al. (2022), who developed this dataset for LSST using a modified run of TRILEGAL (Girardi et al. 2012). The catalog photometry is provided in the LSST bands and these were converted to the DES bands, similar to what is done in Yamamoto & Becker et al. (2025). For each simulated coadd tile, we select all stars whose positions in the TRILEGAL catalog are within the tile boundaries. However, we then randomly draw new positions (from a uniform distribution

in coadd pixel coordinates) for each star and use this as the location of the injection. For binary star systems in the catalog, we also randomly sample the positional angle of the system on the sky. Similar to the galaxy injections, we subselect stars with $i < 25.5$ to form our injection sample.

Extinction: All objects are reddened during injection. The extinction coefficients, $E(B - V)$ are taken from Schlegel et al. (1998). The reddening coefficients, A_b , for band b , are 2.140, 1.569, 1.196 for the riz bands, respectively (DES Collaboration et al. 2018, see their Section 4.2). We obtain the reddened magnitudes, $m_b = m_{b,0} + A_b \times E(B - V)$, by computing $A_b \times E(B - V)$ at the sky location of each object we inject.

Simulating individual CCD images: Once we have defined the shapes and location of galaxies — and also the locations of the stars — on the coadd tile, we simulate the individual CCD images that contribute to the coadd image. The objects are rendered as GALSIM models and then convolved with the PSFEX model of that CCD image, where the latter model is evaluated at the location of the injection. These PSF-convolved galaxy models are drawn onto an CCD image that is initially blank. We then add to it the background and noise associated with the original image. The noise is simulated using the image weights given the latter is an estimate of the noise variance. The simulated image is also assigned the same weights and mask as the original.

Generating coadd image: The individual images are passed through a pixel-correction step with DESDM, called `coadd_nwgin`, and these processed images are then coadded using the SWARP (Bertin 2010) algorithm to form coadd images for each of the three bands (r, i, z). The images from the three bands are then coadded again, using SWARP, to form the detection coadd.

SOURCEEXTRACTOR object catalogs and MEDS files: The detection coadd is analyzed using SOURCEEXTRACTOR (Bertin & Arnouts 1996) to obtain the object catalog. The algorithm is then run three more times in “dual mode” to get the object properties (photometry, size etc.) in each of the three bands. This catalog, alongside the simulated images, is used to create a multi-epoch data structure file (MEDS, Jarvis et al. 2016) for the coadd tile.

METACALIBRATION: Finally, we process the simulated MEDS file through the same shape measurement pipeline as that used on the data (see Section 3.1).

At the end of this process, each simulated coadd tile will have two catalogs associated with it. One from a simulation where all galaxies are sheared with $\gamma_1 = +0.02$ and another with $\gamma_1 = -0.02$. Both simulations contain the same rotated galaxies, noise realisations etc. and differ only in the applied

external shear. Together, the two runs are used to estimate the multiplicative bias m via the variance cancellation technique of Pujol et al. (2019). This cancellation is done by using both versions of the tile to estimate the shear of the sample,

$$\gamma_i^{\text{est}} = \frac{\langle e^+ \rangle - \langle e^- \rangle}{2\langle R \rangle}, \quad (21)$$

where $\langle e^\pm \rangle$ is the mean ellipticity in the simulation with $\gamma_{1\pm} = \pm 0.02$, and $\langle R \rangle = \langle R^+ \rangle + \langle R^- \rangle$. Since both simulated versions only differ in the external shear applied to galaxies, all noise factors can be suppressed by taking the difference between the two. In practice, we find the estimator in Equation (21) improves our precision by at least a factor of 2, and often more. Once γ_i^{est} is estimated, we can infer m using Equation (20) with $\gamma_1^{\text{true}} = 0.02$. We always use γ_1 (γ_2) for estimating the multiplicative (additive) bias. The uncertainties on m and c are obtained through jackknife resampling by dropping the objects from one coadd tile at a time.

Our image simulation pipeline is also modified to perform synthetic source injection — analogous to the synthetic source injection pipeline in DES denoted as “BALROG” (Suchyta et al. 2016; Everett et al. 2022; Anbajagane & Tabbutt et al. 2025) — and is used for the photometric redshift calibration presented in PAPER II. In that work, we run our pipeline on the real (not simulated) CCD images from DECam and show we reproduce the object fits from the DESDM pipeline, which is a validation our pipeline accurately mimics the one used on the real data.

5.2 Validation

The image simulations use an extensive, multi-faceted pipeline. In PAPER II, we show that our pipeline matches the image processing done on the actual data. However, there are still additional subtleties involved with simulating synthetic sources. Past works have performed an end-to-end validation of their simulations by checking the pipeline produces small multiplicative biases, in specific, idealized cases. We show these results in Section 5.2.1. Furthermore, we check the realism of our simulated dataset in Section 5.2.2 by comparing the properties of simulated galaxies with those of the real galaxies in our data.

5.2.1 Unit tests

Following MacCrann & Becker et al. (2022), we perform a number of units tests to validate the simulation pipeline. This involves running the simulation pipeline in a series of simplistic settings. The galaxies in these tests are all placed on a square grid (*i.e.*, there is no blending of galaxies) and they have exponential profiles, with half-light radii that we either fix to $0.5''$ or vary by sampling radii from the Cosmos catalog. In the latter case, we always limit the maximum radii to $1''$

No.	mag	size	PSF	Mask	$m (10^{-3}, 3\sigma)$
1	17	$0.5''$	$0.9''$ (Gauss)	No	0.146 ± 0.486
2	17	$0.5''$	PSFEX	No	-0.006 ± 0.413
3	17	variable	PSFEX	No	0.040 ± 0.326
4	20	variable	PSFEX	No	0.001 ± 0.416
5	17	variable	PSFEX	Yes	-0.080 ± 0.351

Table 3. Results for the validation tests on the simulation pipeline that is then used to calibrate the shear measurements. All unit tests show $m < 10^{-3}$ with $> 3\sigma$ confidence, indicating the pipeline is robust. See Section 5.2 for details on the tests.

in order to prevent overlap in galaxy injections. All injected galaxies also have the same brightness in all three bands (riz), and we vary the galaxy magnitude in different runs. We test one run where the PSF is a Gaussian with FWHM of $0.9''$, while the rest of the runs use the fiducial PSFEX model used in the main simulations. In all validation runs, we do not perform SOURCEEXTRACTOR detection, as any such detection step can introduce a shear-dependent detection that will lead to residual multiplicative biases (MacCrann & Becker et al. 2022, see their Section 4). Instead, we run the pipeline in “true detection” mode where the exact injected locations of objects are passed back into the pipeline as a detection catalog. This is done *only* for the unit tests in this subsection. The fiducial run, whose results are discussed in Section 5.3, include the SOURCEEXTRACTOR step as part of the full DESDM pipeline.

Table 3 shows the results from our unit tests. We show only the multiplicative bias, m , as it is the key quantity to validate. The order-of-magnitude expectation for the minimum bias in the simulated lensing signal is $m \sim \gamma_1^2 \sim 10^{-4}$, which arises because our shear estimator ignores terms that are quadratic, or higher, in γ_1 (Bernstein et al. 2016; Sheldon & Huff 2017). Our unit tests show the multiplicative bias is below $m < 10^{-3}$ at $> 3\sigma$ significance, which is the requirement for our validation, and some tests find no bias down to the 10^{-4} level. The additive bias, c , is not quoted above but is at/below 10^{-4} for all simulation versions, similar to the amplitudes seen in previous works (MacCrann & Becker et al. 2022, see their Table B1).

5.2.2 Comparing image simulations with data

While Section 5.2.1 validated the simulation pipeline, an equally important validation is checking that the object catalog from the simulations is representative of the actual data. Figure 15 shows a corner plot comparing the distributions of the METACALIBRATION properties in the simulations and in the data. Both samples have no selections applied to them. The 2D distributions show the 1σ , 2σ , and 3σ contours. The 1D distributions along the diagonal show an excellent match between simulations and data; the sole exception is the size distributions where the simulations show a deficit of

large objects (high T values). This is a known difference, arising from the rarity of large objects and only a few of them being present in the COSMOS region of the sky from which our injection sample is derived (Hartley & Choi et al. 2022; MacCrann & Becker et al. 2022). Note that the 1D distributions are presented on a *logarithmic* scale, and thus the difference is amplified visually. On the other hand, the 68% and 95% contours of the distributions are on top of each other, showcasing an excellent match. Thus, while there is indeed a deficit of large objects in the simulated catalogs, the majority of the catalog is still representative of the data. Therefore, the simulations match the data and therefore can be relied on for calibrating the shear estimates.

A salient point is also the realism of the PSF used in our image simulation. In our simulation pipeline, the PSF_{EX} model is assumed to be the true PSF; we generate mock observations of a galaxy using the PSF_{EX} model and analyze said observations using the exact same model. Any systematic bias in the former (and therefore any downstream effects of the bias on the final shear calibration) will not be captured in the simulations due to this assumption. We have already presented some signs of such an error, in Figure 6 and Figure 7. However, we now explicitly compute the average size error for our galaxy sample, by using the $1 - T_{\text{psf}}/T_{\star}$ of our PSF star sample and calculating a weighted average across the catalog. The weights are the star weights discussed previously which upweight the signal at the location of galaxies. We find the size error is -0.2% , *i.e.*, the PSF model is on average 0.2% larger than the size of the stars.

We check the impact of this mean error by simulating it in our pipeline: we continue to convolve the galaxy with the PSF_{EX} model before injection, but provide a slightly smaller PSF to METACALIBRATION during the shape fitting procedure. The recovered multiplicative bias is $m = (2.6 \pm 0.2) \times 10^{-3}$, which is within the uncertainties of our shear calibration as we will discuss below.

5.3 Final shear calibration

For the final calibration of the data, we take the 1600 tiles of our fiducial simulation run and compute the multiplicative bias using only galaxies that pass the cuts discussed in Section 3. We replicate all cuts described in that section, with the sole exception of the FITVD failure cut which is left out as we do not run FITVD fitting in our pipeline. This minor mismatch, of not using FITVD flags, is similar to that done in the DES Y3 calibration work (MacCrann & Becker et al. 2022).

Furthermore, we require a calibration factor per tomographic redshift bin. These bins have been defined in PAPER II by using self-organizing maps (SOMs; Kohonen 1982; Kohonen 2001), which were trained on galaxy

	m (10^{-2})	c (10^{-4})
Bin 1	-0.923 ± 0.296	-4.966 ± 1.788
Bin 2	-1.895 ± 0.421	-5.681 ± 1.764
Bin 3	-4.004 ± 0.428	-3.812 ± 1.542
Bin 4	-3.733 ± 0.462	-7.273 ± 1.688
Full sample	-2.454 ± 0.124	-5.262 ± 0.959

Table 4. The multiplicative calibration factor for the four tomographic bins and the full sample, as determined by the image simulations suite developed in this work. The calibration values are similar to those of DES Y3 (MacCrann & Becker et al. 2022). We also show the additive terms, c , which are also similar (but slightly higher than) that work.

photometry, to assign galaxies to tomographic bins. We take the SOM built from the data and use it to assign simulated galaxies — via their METACALIBRATION photometry estimates — to the four tomographic bins. We then estimate the multiplicative bias in each bin using Equation (20) and Equation (21). Note that when making these estimates, all simulated galaxies are assigned weights using the 2D grid defined in Section 3.3, and the final calibration per bin is obtained via weighted averages of the relevant quantities.

Table 4 shows our final results for the calibration factors. Our estimates for m have a similar amplitude to that of MacCrann & Becker et al. (2022, see their Table 3). We note also that our estimate of m in bin 3 has a higher amplitude than that of m in bin 4, but the two estimates are only 0.5σ from each other so this ordering is not statistically significant. We also note that our estimate of the additive bias, c — which is extracted from the simulations using measurements of γ_2 — has a somewhat similar amplitude as the mean shear of γ_2 measured in the data (see Table 2).

We briefly note that the DES Y3 image simulations campaign (MacCrann & Becker et al. 2022) also derived a modified m that — in addition to the effects discussed above — accounted for the impact of blending on the source-galaxy redshift distributions. See their Section 2.3 and 2.4 for more details. Amon et al. (2022, see their Figure 11) show that this additional correction has negligible impact on the cosmology constraints given the precision of the DES Y3 sample. Thus, in this work we do not incorporate this additional correction.

6 SUMMARY

In this paper we present the DECADE shape catalog, which contains 107 million galaxies covering $5,412 \text{ deg}^2$ in the northern Galactic cap region. The catalog is derived from public DECam imaging data, coming from both large survey programs as well as smaller, standard observing programs. The object shapes are measured using the METACALIBRATION methodology, and the final source sample is tailored for cosmological analyses with weak lensing. The effective

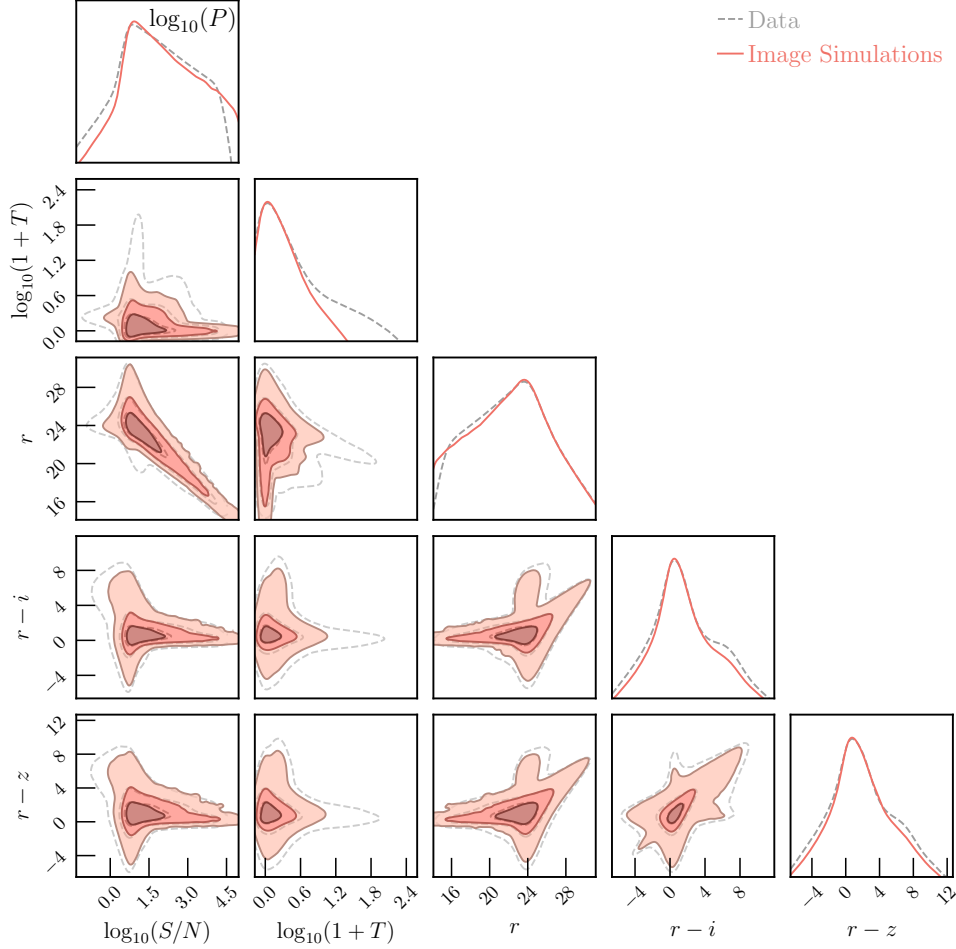


Figure 15. Distribution of METACALIBRATION properties of objects from the simulations (red) and data (grey). We use the raw catalogs and have not applied our selection function. The contours show the 1σ , 2σ , and 3σ regions. The 1D distributions along the diagonal are the log probability. The simulations are an excellent match to the data until the 2σ region, and generally still a good match up to 3σ , with the largest deviations coming from the fact that the COSMOS catalog used for simulated injections lacks large (high T) objects. Note that this is the raw catalog with no cuts.

number density of the full source-galaxy sample is 4.56 galaxies per arcmin², and the sample has a statistical precision similar to that of the DES Y3 shape catalog (GS21).

To ensure the robustness of this shape catalog, we perform a series of empirical tests including: (1) the mean PSF shape in focal plane coordinates, (2) the residual brighter-fatter effect, (3) the color-dependence of the PSF shape, (4) the mean shear as a function of METACALIBRATION quantities, (5) the two-point functions of the PSF and galaxy shapes, also known as Rowe statistics and Tau statistics, (6) the tangential shear around stars and field centers, (7) the spatial correlation of the mean shear and various survey properties, and (8) the B -mode signals. Overall, we find that the residual systematic effects derived from these tests are either subdominant relative to our signal, or are statistically insignificant. An explicit test of the PSF-related contamination in PAPER III also shows the PSF contamination, as estimated from the Rowe and Tau stats,

has a completely negligible bias in the derived cosmological constraints.

In parallel we build an image simulation pipeline to both test our METACALIBRATION estimator and to quantify the shear calibration bias (and its uncertainty). The latter is done both for the full sample as well as for the four tomographic redshift bins as defined in PAPER II. We find an overall shear calibration bias of $m \approx 2.5\%$, with the calibrations for each tomographic bins being within $\approx 1\%$ of this value. These level of multiplicative biases are comparable to other state-of-the-art weak lensing shear measurements, and particularly to the METACALIBRATION-based measurements of DES Y3 (MacCrann & Becker et al. 2022). The results from our null-tests and the shear calibration indicate it is possible to construct a lensing dataset with similar robustness to that of DES Y3, but while using image data that have significant spatial inhomogeneity and variability in data quality, and that

were observed at high airmass. This has implications for the kinds of data that can be incorporated into datasets in upcoming lensing surveys such as Rubin LSST and the *Nancy Grace Roman Space Telescope*.

We briefly note that the coadded images and catalogs created by the DECADE cosmic shear project have uses for many astronomical science goals beyond just cosmic shear. In particular, we have assembled a deep, well-tested, multi-band object catalog (see [Tan et al. 2024](#)) and value-added products such as a shape catalog (this work) and photometric redshift distributions (see [PAPER II](#)). The coadded images themselves enable a wide suite of science analyses. The DECADE shape catalog will be made publicly available upon publication of the cosmology results, while the coadded images and object catalogs associated with this shape catalog will be part of the forthcoming DELVE Early Data Release 3.

Finally, as mentioned before, this work is part of a series of papers within the DECADE project. The others detail the redshift estimates ([PAPER II](#)), the analysis methodology and survey inhomogeneity tests ([PAPER III](#)), and the cosmology results for the DECADE catalog ([PAPER IV](#)). This work was also limited to image data only in the northern Galactic cap (“DELVE Early Data Release 3”). We have already processed public DECam data in the southern Galactic cap, surrounding the DES footprint. These shape measurements (as well as all other necessary calibrations and data products) cover an additional $\approx 3,300 \text{ deg}^2$ and will be presented in the near future. The work in this series of papers sets the stage for performing a cosmic shear analysis across $13,000 \text{ deg}^2$ of the sky, using only DECam data. Once completed, the dataset will more than double the sky coverage of existing, precision weak lensing surveys and therefore, will improve their synergies with many ongoing and upcoming surveys.

ACKNOWLEDGEMENTS

DA is supported by the National Science Foundation (NSF) Graduate Research Fellowship under Grant No. DGE 1746045. CC is supported by the Henry Luce Foundation and Department of Energy (DOE) grant DE-SC0021949. The DECADE project is supported by NSF AST-2108168 and AST-2108169. The DELVE Survey gratefully acknowledges support from Fermilab LDRD (L2019.011), the NASA *Fermi* Guest Investigator Program Cycle 9 (No. 91201), and the NSF (AST-2108168, AST-2108169, AST-2307126, AST-2407526, AST-2407527, AST-2407528). This work was completed in part with resources provided by the University of Chicago’s Research Computing Center. The project that gave rise to these results received the support of a fellowship from “la Caixa” Foundation (ID 100010434). The fellowship code is LCF/BQ/PI23/11970028. C.E.M.-V. is supported by the international Gemini Observatory, a program

of NSF NOIRLab, which is managed by the Association of Universities for Research in Astronomy (AURA) under a cooperative agreement with the U.S. National Science Foundation, on behalf of the Gemini partnership of Argentina, Brazil, Canada, Chile, the Republic of Korea, and the United States of America.

Funding for the DES Projects has been provided by the U.S. Department of Energy, the U.S. National Science Foundation, the Ministry of Science and Education of Spain, the Science and Technology Facilities Council of the United Kingdom, the Higher Education Funding Council for England, the National Center for Supercomputing Applications at the University of Illinois at Urbana-Champaign, the Kavli Institute of Cosmological Physics at the University of Chicago, the Center for Cosmology and Astro-Particle Physics at the Ohio State University, the Mitchell Institute for Fundamental Physics and Astronomy at Texas A&M University, Financiadora de Estudos e Projetos, Fundação Carlos Chagas Filho de Amparo à Pesquisa do Estado do Rio de Janeiro, Conselho Nacional de Desenvolvimento Científico e Tecnológico and the Ministério da Ciência, Tecnologia e Inovação, the Deutsche Forschungsgemeinschaft and the Collaborating Institutions in the Dark Energy Survey.

The Collaborating Institutions are Argonne National Laboratory, the University of California at Santa Cruz, the University of Cambridge, Centro de Investigaciones Energéticas, Medioambientales y Tecnológicas-Madrid, the University of Chicago, University College London, the DES-Brazil Consortium, the University of Edinburgh, the Eidgenössische Technische Hochschule (ETH) Zürich, Fermi National Accelerator Laboratory, the University of Illinois at Urbana-Champaign, the Institut de Ciències de l’Espai (IEEC/CSIC), the Institut de Física d’Altes Energies, Lawrence Berkeley National Laboratory, the Ludwig-Maximilians Universität München and the associated Excellence Cluster Universe, the University of Michigan, NSF’s NOIRLab, the University of Nottingham, The Ohio State University, the University of Pennsylvania, the University of Portsmouth, SLAC National Accelerator Laboratory, Stanford University, the University of Sussex, Texas A&M University, and the OzDES Membership Consortium.

The DES data management system is supported by the National Science Foundation under Grant Numbers AST-1138766 and AST-1536171. The DES participants from Spanish institutions are partially supported by MICINN under grants ESP2017-89838, PGC2018-094773, PGC2018-102021, SEV-2016-0588, SEV-2016-0597, and MDM-2015-0509, some of which include ERDF funds from the European Union. IFAE is partially funded by the CERCA program of the Generalitat de Catalunya. Research leading to these results has received funding from the European Research Council

under the European Union’s Seventh Framework Program (FP7/2007-2013) including ERC grant agreements 240672, 291329, and 306478. We acknowledge support from the Brazilian Instituto Nacional de Ciência e Tecnologia (INCT) do e-Universo (CNPq grant 465376/2014-2).

Based in part on observations at Cerro Tololo Inter-American Observatory at NSF’s NOIRLab, which is managed by the Association of Universities for Research in Astronomy (AURA) under a cooperative agreement with the National Science Foundation.

This work has made use of data from the European Space Agency (ESA) mission *Gaia* (<https://www.cosmos.esa.int/gaia>), processed by the *Gaia* Data Processing and Analysis Consortium (DPAC, <https://www.cosmos.esa.int/web/gaia/dpac/consortium>). Funding for the DPAC has been provided by national institutions, in particular the institutions participating in the *Gaia* Multilateral Agreement.

This paper is based on data collected at the Subaru Telescope and retrieved from the HSC data archive system, which is operated by the Subaru Telescope and Astronomy Data Center (ADC) at NAOJ. Data analysis was in part carried out with the cooperation of Center for Computational Astrophysics (CfCA), NAOJ. We are honored and grateful for the opportunity of observing the Universe from Maunakea, which has the cultural, historical and natural significance in Hawaii.

This manuscript has been authored by Fermi Forward Discovery Group, LLC under Contract No. 89243024CSC000002 with the U.S. Department of Energy, Office of Science, Office of High Energy Physics.

All analysis in this work was enabled greatly by the following software: PANDAS (McKinney 2011), NUMPY (Van der Walt et al. 2011), SCIPY (Virtanen et al. 2020), and MATPLOTLIB (Hunter 2007). We have also used the Astrophysics Data Service (ADS) and arXiv preprint repository extensively during this project and the writing of the paper.

DATA AVAILABILITY

All catalogs and derived data products (data vectors, redshift distributions, calibrations etc.) will be made public upon acceptance of the cosmology results.

REFERENCES

- Ade P., et al., 2019, *J. Cosmology Astropart. Phys.*, 2019, 056
 Aihara H., et al., 2018, *PASJ*, 70, S8
 Albrecht A., et al., 2006, *arXiv e-prints*, pp astro-ph/0609591
 Alonso D., Sanchez J., Slosar A., LSST Dark Energy Science Collaboration 2019, *MNRAS*, 484, 4127
 Amon A., et al., 2022, *Phys. Rev. D*, 105, 023514
 Anbajagane & Tabbutt et al., 2025, *arXiv e-prints*, p. arXiv:2501.05683
 Anbajagane D., Pandey S., Chang C., 2024a, *The Open Journal of Astrophysics*, 7, 108
 Anbajagane D., et al., 2024b, *MNRAS*, 527, 9378
 Anbajagane D., Chang C., Lee H., Gatti M., 2024c, *J. Cosmology Astropart. Phys.*, 2024, 062
 Anbajagane D., et al., 2025c, *arXiv e-prints*
 Anbajagane D., et al., 2025b, *arXiv e-prints*
 Anbajagane D., et al., 2025a, *arXiv e-prints*
 Antilogus P., Astier P., Doherty P., Guyonnet A., Regnault N., 2014, *Journal of Instrumentation*, 9, C03048
 Aricò G., Angulo R. E., Contreras S., Ondaro-Mallea L., Pellejero-Ibañez M., Zennaro M., 2021, *MNRAS*, 506, 4070
 Asgari M., et al., 2021, *A&A*, 645, A104
 Bacon D. J., Refregier A. R., Ellis R. S., 2000, *MNRAS*, 318, 625
 Bartelmann M., Schneider P., 2001, *Phys. Rep.*, 340, 291
 Bechtol K., et al., 2025, *arXiv e-prints*, p. arXiv:2501.05739
 Becker M. R., Rozo E., 2016, *MNRAS*, 457, 304
 Bernstein G. M., Armstrong R., 2014, *MNRAS*, 438, 1880
 Bernstein G. M., Armstrong R., Krawiec C., March M. C., 2016, *MNRAS*, 459, 4467
 Bernstein G. M., et al., 2017a, *PASP*, 129, 074503
 Bernstein G. M., et al., 2017b, *PASP*, 129, 114502
 Bernstein G. M., et al., 2018, *PASP*, 130, 054501
 Bertin E., 2010, SWarp: Resampling and Co-adding FITS Images Together, Astrophysics Source Code Library, record ascl:1010.068
 Bertin E., 2013, PSFEx: Point Spread Function Extractor, Astrophysics Source Code Library, record ascl:1301.001 (ascl:1301.001)
 Bertin E., Arnouts S., 1996, *A&AS*, 117, 393
 Bianco F. B., et al., 2022, *ApJS*, 258, 1
 Bigwood L., et al., 2024, *arXiv e-prints*, p. arXiv:2404.06098
 Bocquet S., et al., 2024, *Phys. Rev. D*, 110, 083510
 Bridle S., et al., 2010, *MNRAS*, 405, 2044
 Carlstrom J. E., et al., 2011, *PASP*, 123, 568
 Cawthon R., et al., 2022, *MNRAS*, 513, 5517
 Chang C., et al., 2013, *MNRAS*, 434, 2121
 Chang C., et al., 2019, *MNRAS*, 482, 3696
 Chang C., et al., 2023, *Phys. Rev. D*, 107, 023530
 Chisari N. E., et al., 2018, *MNRAS*, 480, 3962
 DES & KiDS Collaborations et al., 2023, *arXiv e-prints*, p. arXiv:2305.17173
 DES Collaboration et al., 2018, *ApJS*, 239, 18
 DES Collaboration Abbott T. M. C., et al., 2021, *ApJS*, 255, 20
 DESI Collaboration et al., 2016, *arXiv e-prints*, p. arXiv:1611.00036
 Dal Tio P., et al., 2022, *ApJS*, 262, 22
 Dalal R., et al., 2023, *arXiv e-prints*, p. arXiv:2304.00701
 Dey A., et al., 2019, *AJ*, 157, 168
 Diehl H. T., Yanny B., Tucker D. L., Paz-Chinchón F., Neilsen E., et al., 2019, Technical report, The Dark Energy Survey and Operations: Year 6 – The Finale. Fermilab, doi:10.2172/1596042
 Drlica-Wagner A., et al., 2018, *ApJS*, 235, 33
 Drlica-Wagner A., et al., 2021, *ApJS*, 256, 2
 Drlica-Wagner A., et al., 2022, *ApJS*, 261, 38
 Estrada J., et al., 2010, in McLean I. S., Ramsay S. K., Takami H., eds, Society of Photo-Optical Instrumentation Engineers (SPIE) Conference Series Vol. 7735, Ground-based and Airborne Instrumentation for Astronomy III. p. 77351R, doi:10.1117/12.857651
 Everett S., et al., 2022, *ApJS*, 258, 15
 Flaugher B., et al., 2015, *AJ*, 150, 150

- Foreman-Mackey D., Hogg D. W., Lang D., Goodman J., 2013, *PASP*, **125**, 306
- Fowler J. W., et al., 2007, *Appl. Opt.*, **46**, 3444
- Gaia Collaboration et al., 2021, *A&A*, **649**, A1
- Gatti & Sheldon et al., 2021, *MNRAS*, **504**, 4312
- Giannini G., et al., 2022, *arXiv e-prints*, p. arXiv:2209.05853
- Giblin B., et al., 2021, *A&A*, **645**, A105
- Girardi L., et al., 2012, in *Red Giants as Probes of the Structure and Evolution of the Milky Way*. p. 165, doi:10.1007/978-3-642-18418-5_17
- Goldstein S., Philcox O. H. E., Hill J. C., Hui L., 2024, *Phys. Rev. D*, **110**, 083516
- Górski K. M., Hivon E., Banday A. J., Wandelt B. D., Hansen F. K., Reinecke M., Bartelmann M., 2005, *ApJ*, **622**, 759
- Grandis S., Aricò G., Schneider A., Linke L., 2024, *MNRAS*, **528**, 4379
- Gruen D., Bernstein G. M., Jarvis M., Rowe B., Vikram V., Plazas A. A., Seitz S., 2015, *Journal of Instrumentation*, **10**, C05032
- Guerrini S., et al., 2024, *arXiv e-prints*, p. arXiv:2412.14666
- Guinot A., et al., 2022, *A&A*, **666**, A162
- Guyonnet A., Astier P., Antilogus P., Regnault N., Doherty P., 2015, *A&A*, **575**, A41
- Harris W. E., 1997, *VizieR Online Data Catalog: Globular Clusters in the Milky Way (Harris, 1997)*, *VizieR On-line Data Catalog: VII/202*. Originally published in: 1996AJ....112.1487H
- Hartlap J., Simon P., Schneider P., 2007, *A&A*, **464**, 399
- Hartley & Choi et al., 2022, *MNRAS*, **509**, 3547
- Heymans C., et al., 2006, *MNRAS*, **368**, 1323
- Heymans C., et al., 2012, *MNRAS*, **427**, 146
- Heymans C., et al., 2013, *MNRAS*, **432**, 2433
- Hirata C., Seljak U., 2003, *MNRAS*, **343**, 459
- Hoffleit D., Jaschek C., 1991, *The Bright star catalogue*
- Hoffleit, D. Warren Jr, W. H. 1991, *The Bright Star Catalogue, 5th Revised Ed. (Preliminary Version)*. Astronomical Data Center, NSSDC/ADC
- Huff E., Mandelbaum R., 2017, *arXiv e-prints*, p. arXiv:1702.02600
- Hunter J. D., 2007, *Computing in Science and Engineering*, **9**, 90
- Jarvis M., Bernstein G., Jain B., 2004, *MNRAS*, **352**, 338
- Jarvis M., et al., 2016, *MNRAS*, **460**, 2245
- Jarvis M., et al., 2020, *arXiv e-prints*, p. arXiv:2011.03409
- Jee M. J., Tyson J. A., Schneider M. D., Wittman D., Schmidt S., Hilbert S., 2013, *ApJ*, **765**, 74
- Kacprzak T., Fluri J., Schneider A., Refregier A., Stadel J., 2023, *J. Cosmology Astropart. Phys.*, **2023**, 050
- Kaiser N., Wilson G., Luppino G. A., 2000, *ArXiv Astrophysics e-prints*,
- Kitching T. D., et al., 2012, *MNRAS*, **423**, 3163
- Kohonen T., 1982, *Biological Cybernetics*, **43**, 59
- Kohonen T., 2001, *Self-Organizing Maps*
- LSST Science Collaboration et al., 2009, *arXiv e-prints*, p. arXiv:0912.0201
- Li X., Mandelbaum R., 2023, *MNRAS*, **521**, 4904
- Li X., et al., 2022, *PASJ*, **74**, 421
- Longley E. P., et al., 2023, *MNRAS*, **520**, 5016
- MacCrann & Becker et al., 2022, *MNRAS*, **509**, 3371
- Makarov D., Prugniel P., Terekhova N., Courtois H., Vauglin I., 2014, *A&A*, **570**, A13
- Mandelbaum R., 2018, *ARA&A*, **56**, 393
- Mandelbaum R., et al., 2005, *MNRAS*, **361**, 1287
- Mandelbaum R., et al., 2015, *MNRAS*, **450**, 2963
- McKinney W., 2011, *Python for High Performance and Scientific Computing*, 14
- Ménard B., Scranton R., Schmidt S., Morrison C., Jeong D., Budavari T., Rahman M., 2013, *arXiv e-prints*, p. arXiv:1303.4722
- Meyers J. E., Burchat P. R., 2015, *ApJ*, **807**, 182
- Morganson E., et al., 2018, *PASP*, **130**, 074501
- Myles & Alarcon et al., 2021, *MNRAS*, **505**, 4249
- Neilsen E., Bernstein G., Gruendl R., Kent S., 2016, Technical Report FERMILAB-TM-2610-AE-CD, "Limiting magnitude, τ , T_{eff} , and image quality in DES Year 1", <https://www.osti.gov/biblio/1250877>. Fermi National Accelerator Laboratory, doi:10.2172/1250877, <https://www.osti.gov/biblio/1250877>
- Neilsen Eric H. J., Annis J. T., Diehl H. T., Swanson M. E. C., D'Andrea C., Kent S., Drlica-Wagner A., 2019, Technical Report FERMILAB-TM-2714-AE-CD-PPD, "Dark Energy Survey's Observation Strategy, Tactics, and Exposure Scheduler". (arXiv:1912.06254), doi:10.2172/1574836
- Newman J. A., 2008, *ApJ*, **684**, 88
- Omori Y., et al., 2019, *Phys. Rev. D*, **100**, 043501
- Pandey S., et al., 2019, *Phys. Rev. D*, **100**, 063519
- Paulin-Henriksson S., Amara A., Voigt L., Refregier A., Bridle S. L., 2008, *A&A*, **484**, 67
- Plazas A. A., Bernstein G., 2012, *PASP*, **124**, 1113
- Plazas A. A., Bernstein G. M., Sheldon E. S., 2014a, *Journal of Instrumentation*, **9**, C04001
- Plazas A. A., Bernstein G. M., Sheldon E. S., 2014b, *PASP*, **126**, 750
- Pujol A., Kilbinger M., Sureau F., Bobin J., 2019, *A&A*, **621**, A2
- Rowe B., 2010, *MNRAS*, **404**, 350
- Rowe B. T. P., et al., 2015, *Astronomy and Computing*, **10**, 121
- Samuroff S., et al., 2023, *MNRAS*, **524**, 2195
- Sánchez J., et al., 2022, *arXiv e-prints*, p. arXiv:2210.08633
- Schlegel D. J., Finkbeiner D. P., Davis M., 1998, *ApJ*, **500**, 525
- Schmidt F., 2008, *Phys. Rev. D*, **78**, 043002
- Schneider P., 2005, *arXiv e-prints*, pp astro-ph/0509252
- Schneider M., Knox L., Zhan H., Connolly A., 2006, *ApJ*, **651**, 14
- Schneider P., Eifler T., Krause E., 2010, *A&A*, **520**, A116
- Schneider A., Teyssier R., Stadel J., Chisari N. E., Le Brun A. M. C., Amara A., Refregier A., 2019, *J. Cosmology Astropart. Phys.*, **2019**, 020
- Schutt T., et al., 2025, *arXiv e-prints*, p. arXiv:2501.05781
- Scoville N., et al., 2007, *ApJS*, **172**, 1
- Secco & Samuroff et al., 2022, *Phys. Rev. D*, **105**, 023515
- Sevilla-Noarbe I., et al., 2021, *ApJS*, **254**, 24
- Sheldon E. S., 2014, *MNRAS*, **444**, L25
- Sheldon E., 2015, *NGMIX: Gaussian mixture models for 2D images*, Astrophysics Source Code Library, record ascl:1508.008
- Sheldon E. S., Huff E. M., 2017, *ApJ*, **841**, 24
- Sheldon E. S., Becker M. R., MacCrann N., Jarvis M., 2020, *ApJ*, **902**, 138
- Shin T., et al., 2019, *MNRAS*, **487**, 2900
- Skrutskie M. F., et al., 2006, *AJ*, **131**, 1163
- Suchyta E., et al., 2016, *MNRAS*, **457**, 786
- Tan C. Y., Cerny W., Drlica-Wagner A., Ji A. P., Li T. S., Pace A., Adamow M., others 2024, submitted to AAS Journals
- Thornton R. J., et al., 2016, *ApJS*, **227**, 21
- Van der Walt S., Colbert S. C., Varoquaux G., 2011, *Computing in Science and Engineering*, **13**, 22
- Vikram V., Lidz A., Jain B., 2017, *MNRAS*, **467**, 2315
- Virtanen P., et al., 2020, *Nature Methods*, **17**, 261
- Vivas K., Walker A., 2023, *The NOIRLab Mirror*, **4**, 23
- Wittman D. M., Tyson J. A., Kirkman D., Dell'Antonio I., Bernstein G., 2000, *Nature*, **405**, 143
- Yamamoto & Becker et al., 2025, *arXiv e-prints*, p. arXiv:2501.05665
- York D. G., et al., 2000, *The Astronomical Journal*, **120**, 1579
- Zhang T., et al., 2023, *MNRAS*, **525**, 2441
- Zuntz & Sheldon et al., 2018, *MNRAS*, **481**, 1149
- de Jong J. T. A., et al., 2015, *A&A*, **582**, A62

A PSF MODELING

There are several aspects of the PSF modeling and testing in this work that are different from that of the DES Y3 analysis (Jarvis et al. 2020). We describe here the details of our PSF modeling procedure and our validation that the models are sufficiently accurate for the cosmology analysis.

A1 PSF star selection

The PSF model of a given CCD image is estimated using a subset of stars from that image that are well-suited for constructing the PSF. For example, common considerations are choosing stars that are sufficiently bright to be a good, high signal-to-noise measure of the PSF, but that are not too bright to suffer saturation or other significant non-linearities in the detectors (*e.g.*, Jarvis et al. 2020). In this work, the star selection follows the algorithm internal to PSFEX, with the settings shown in Table A1.

The PSF star catalog is obtained from an initial SOURCEEXTRACTOR run of the CCD image, where this initial run is optimized for finding bright stars and is thus different from the run performed on the coadd images. See Morganson et al. (2018, section 4.5) for more details. This catalog is then postprocessed internally within PSFEX. The first step places a number of cuts on the PSF star properties from SOURCEEXTRACTOR:

- **Signal-to-noise cut:** The algorithm selects $\text{SNR_WIN} = \text{FLUX_WIN}/\text{FLUXERR_WIN} > \text{SAMPLE_MINSN}$. Here “WIN” indicates that the photometry is calculated with a Gaussian window function, where the width of the Gaussian is defined using the object’s half-light radius.
- **Size cuts:** PSFEX selects all objects with FWHM in the range given by SAMPLE_FWHMRANGE (in pixel units). It then iteratively shrinks the upper and lower bounds of this range until the remaining objects have FWHM values that vary within 20%. The FWHM used is simply twice the FLUX_RADIUS as computed by SOURCEEXTRACTOR.
- **Ellipticity cut:** PSFEX removes all objects with ellipticity larger than SAMPLE_MAXELLIP .

The second selection step occurs during PSF model building. This is performed iteratively, where

- The PSF model is estimated.
- The PSF model is compared with the measurements from the PSF stars

- If any PSF star exhibits a large χ^2 between its measurement and the model, the star is considered an outlier and removed.
- The PSF model is estimated again without these outliers.
- The above steps are performed three times in total, with the χ^2 threshold being halved with each iteration.

This selection procedure is somewhat different from DES Y3 and results in a larger PSF star sample that goes to lower signal-to-noise. In DES Y3, the star selection is part of the PIFF algorithm (Jarvis et al. 2020). In PIFF, after a rough selection in the size and magnitude plane, the algorithm first identifies the brightest 10% of the objects (excluding saturated objects) and finds a narrow locus at small object-size for the stars and a broad locus of galaxies with larger object sizes. Then the algorithm proceeds to fainter magnitudes, building up both loci, until the stellar locus and the galaxy locus start to merge.

We note that there are two additional factors to consider here. First, in the PSFEX model-fitting step each star is effectively weighted by its signal-to-noise. So, the subsample of faint PSF stars does not contribute as much to the model building, and most of the brighter stars will be those found and used in PIFF. Second, due to the unique characteristics of our dataset, there is both (i) more variation in the depth between exposures and (ii) more exposures located closer to the Galactic plane. These two factors contribute to a wider spread in the number of PSF stars in our data as well as a higher number on average. The higher number counts of PSF stars is not an obvious concern for weak lensing analysis, and our PSF tests — such as the Rowe and Tau statistics (Section 4.5) and tangential shear around stars (Section 4.6) — show our PSF model is performing adequately.

A2 The PSF model

PSFEX uses the cutout images of each PSF star selected above in the dimension of PSF_SIZE , and decomposes them into Principal Component Analysis (PCA) elements – each star is now represented by a linear combination of Principle Components (PCs), where we keep only a small number (NEWBASIS_NUMBER) of PCs. Next, PSFEX fits a smooth polynomial function (of order PSFVAR_DEGREES) across each CCD chip to the coefficients of the PCs. This becomes the PSF model for that chip and the PSF at a given location of a galaxy can be reconstructed given the polynomial fit and the PCs.

A3 Reserved stars and PSF tests

In DES Y3, once the star selection is done, a random 20% subset of that selection is set aside and not used for the

PSF model		PSF variability		Sample selection	
Parameter	Value	Parameter	Value	Parameter	Value
BASIS_TYPE	PIXEL	PSFVAR_KEYS	XWIN_IMAGE, YWIN_IMAGE	SAMPLE_AUTOSELECT	Y
BASIS_NUMBER	20	PSFVAR_GROUPS	1,1	SAMPLEVAR_TYPE	SEEING
BASIS_NAME	basis.fits	PSFVAR_DEGREES	2	SAMPLE_FWHMRANGE	2.0,15.0
BASIS_SCALE	1.0	PSFVAR_NSAP	9	SAMPLE_VARIABILITY	0.2
NEWBASIS_TYPE	NONE	HIDDENMEF_TYPE	COMMON	SAMPLE_MINSN	20
NEWBASIS_NUMBER	8	STABILITY_TYPE	EXPOSURE	SAMPLE_MAXELLIP	0.3
PSF_SAMPLING	0.7			SAMPLE_FLAGMASK	0x00fe
PSF_PIXELSIZE	1.0			SAMPLE_IMAFLAGMASK	0x00ff
PSF_ACCURACY	0.01			BADPIXEL_FILTER	N
PSF_SIZE	61,61			BADPIXEL_NMAX	0
CENTER_KEYS	XWIN_IMAGE, YWIN_IMAGE				
PSF_RECENTER	N				
PHOTFLUX_KEY	FLUX_APER(8)				
PHOTFLUXERR_KEY	FLUXERR_APER(8)				
MEF_TYPE	INDEPENDENT				

Table A1. Parameter names and values used in the PSFEx run of the DESDM processing pipeline. All shear measurements in this work (and all PSF tests) derive from the PSF model constructed from PSFEx.

PSF model. This subset serves as a clean sample to test the quality of the PSF model since the objects were not used in constructing the PSF model. In our work, we do not do this step as PSFEx does not provide such a reserve star sample. Furthermore, it was found in DES that the PSF tests (of the kind we perform) are insensitive when swapping the reserved stars sample with the full sample. This is likely because the limiting factor for the quality of the PSF model is usually not the number of stars, but rather the flexibility of the model itself.

To reduce the noise in statistics derived from the e^* and T^* measurements (*e.g.*, the Rowe and Tau statistics in Section 4.5), we place a signal-to-noise cut on the PSF star sample at $\text{SNR_WIN} > 80$. Figure 9 shows an example of variation in the signal-to-noise cut and shows it does not change the qualitative findings of our PSF tests. In addition, our PSF tests (all shown

in Section 4) use a subsampled PSF star catalog rather than the entire catalog. The full catalog is $N \approx 10^9$ in size, and this significantly increases the computational expense of our tests. The PSF tests can be accurately performed with far fewer stars; for example, the DES Y3 tests used $N \sim 10^7$ stars for their tests. In our tests, we reduce the sample size by randomly subsampling 20% of the objects. This subsample is used for all tests and is referred to as the PSF star sample in Section 4.

This paper was built using the Open Journal of Astrophysics L^AT_EX template. The OJA is a journal which provides fast and easy peer review for new papers in the `astro-ph` section of the arXiv, making the reviewing process simpler for authors and referees alike. Learn more at <http://astro.theoj.org>.